Open access • Journal Article • DOI:10.1063/1.1616031

Effect of turbulence on the drag and lift of a particle — Source link

Prosenjit Bagchi, S. Balachandar

Institutions: University of Illinois at Urbana–Champaign

Published on: 01 Oct 2003 - Physics of Fluids (American Institute of Physics)

Topics: Parasitic drag, Drag coefficient, Drag, Zero-lift drag coefficient and Aerodynamic drag

Effect of turbulence on the drag and lift of a particle

P. Bagchi[a] and S. Balachandar[b]
Department of Theoretical and Applied Mechanics, University of Illinois at Urbana–Champaign, Urbana, Illinois 61801

(Received 20 December 2002; accepted 6 August 2003; published 1 October 2003)

A direct numerical simulation (DNS) is used to study the effect of a freestream isotropic turbulent flow on the drag and lift forces on a spherical particle. The particle diameter is about 1.5–10 times the Kolmogorov scale, the particle Reynolds number is about 60–600, and the freestream turbulence intensity is about 10%–25%. The isotropic turbulent field considered here is stationary, i.e., frozen in time. It is shown that the freestream turbulence does not have a substantial and systematic effect on the time-averaged mean drag. The standard drag correlation based on the instantaneous or mean relative velocity results in a reasonably accurate prediction of the mean drag obtained from the DNS. However, the accuracy of prediction of the instantaneous drag decreases with increasing particle size. For the smaller particles, the low frequency oscillations in the DNS drag are well captured by the standard drag, but for the larger particles significant differences exist even for the low frequency components. Inclusion of the added-mass and history forces, computed based on the fluid velocity at the center of the particle, does not improve the prediction. Different estimates of the fluid velocity seen by the particle are examined. It is shown that the mean drag is insensitive to the fluid velocity measured at the particle center, or obtained by averaging over a fluid volume of the order of the particle size. The fluctuations diminish as the size of the averaging volume increases. The effect of increasing freestream turbulence intensity for the same particle size is studied. Fluctuations in the drag and lift forces are shown to scale with the mean drag and freestream intensity. The standard drag without the added-mass and history forces provides the best approximation to the DNS result. © *2003 American Institute of Physics.*
[DOI: 10.1063/1.1616031]

I. INTRODUCTION

Dispersed particulate flows abound in nature and in engineering applications. In most cases, the fluid phase is turbulent. The interaction between the fluid phase and the particulate phase is bidirectional: the carrier-phase turbulence influences the dispersion and preferential accumulation of the particles which in turn modulate the fluid turbulence. At the level of a single particle, the effect of freestream turbulence is to modify the drag force compared to that in a steady uniform flow (often called ''standard drag''). On the other hand, a particle can modify freestream turbulence by the formation of a wake, periodic shedding of vortices, and wake turbulence. The collective effect of the presence of a distribution of particles can further modify the effective drag force on a particle due to screening effect and thereby influence the mean settling and dispersion characteristics. Similarly, the collective effect of the dispersion of particles will determine the attenuation or augmentation of the fluid turbulence.

In this paper we will address the effect of the freestream turbulence on the drag and lift forces on a single particle. We choose to investigate the simplest case of an isotropic freestream turbulence of Taylor microscale Reynolds number equal to 164. The two important parameters of the problem are then the ratio of the particle diameter d to the Kolmogorov scale η, and the intensity of freestream turbulence defined as the ratio of the root-mean-square (rms) turbulent fluctuation to the mean relative velocity between the particle and the surrounding fluid. The diameter of the particle under consideration is varied from about 1 to 10 times the Kolmogorov scale, and the turbulence intensity is varied from 10% to 25%. Consequently the particle Reynolds number, based on the relative velocity and particle diameter, is in the range 60–600.

Consider the case of a particle settling through a turbulent flow. The mean settling velocity of the particle provides a convenient measure of the mean drag force. In experiments the mean drag coefficient is computed based on the measurement of the mean settling velocity V_T and a force balance between the gravity and the drag force as

$$C_D=\frac{4}{3}gd(\rho-1)\frac{1}{V_T^2}, \tag{1}$$

where ρ is the particle-to-fluid density ratio, and g is the acceleration due to gravity. If the ambient flow is stagnant, V_T corresponds to the terminal velocity and the above relation yields the standard drag coefficient corresponding to a uniform nonturbulent flow. In a turbulent flow, however, there are two well-understood mechanisms that influence the mean settling rate. The first is due to the nonlinear depen-

[a]Present address: Department of Mechanical and Aerospace Engineering, Rutgers University, Piscataway, New Jersey 08854.
[b]Author to whom correspondence should be addressed. Electronic mail: s-bala@uiuc.edu

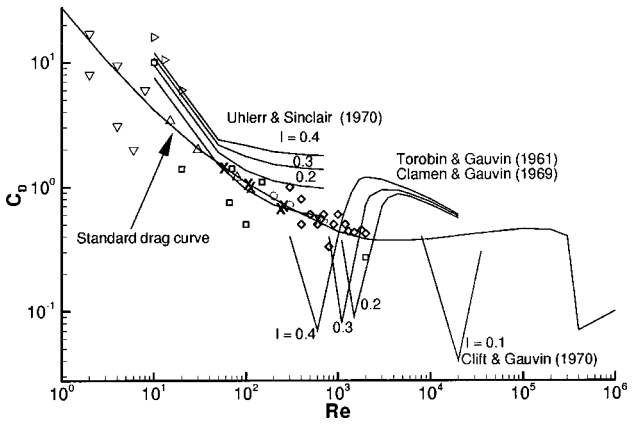

FIG. 1. A summary of the results on the effect of turbulence on the drag coefficient. (×) Present results; (□) Gore and Crowe (Ref. 15); (◇) Sankagiri and Ruff (Ref. 16); (○) Zarin and Nichols (Ref. 4); (△) Warnica *et al.* (Ref. 8); (▽) Rudolf and Bachalo (Ref. 7); (▷) Brucato *et al.* (Ref. 5). The standard drag curve is obtained using the Schiller–Neumann formula, Eq. (2) (see Clift *et al.*—Ref. 18). The parameter I is the ratio of the rms velocity of the freestream turbulence to the mean relative velocity between the particle and the fluid.

dence of the drag on the relative velocity at finite Reynolds numbers. For the same density ratio ρ and diameter d, the mean settling velocity in a turbulent flow is less than that in a stagnant flow (Mei, Adrian, and Hanratty[1]). The settling velocity decreases with increasing turbulence intensity and the resulting mean drag as given by (1) is higher than that based on the terminal velocity in a stagnant flow. This effect will decrease with decreasing Reynolds number and will entirely vanish in the linear Stokes limit. The second, and more complex, mechanism is due to the preferential trajectories of freely falling particles. Particles do not sample the turbulent flow uniformly, but prefer regions of downwash compared to regions of up-moving fluid (see Wang and Maxey[2]). Thus the mean fluid velocity seen by a particle differs from the true mean obtained by averaging over the entire volume of fluid. Unlike the effect of nonlinear drag dependence, the effect of preferential trajectory is to increase the mean settling velocity. Thus the drag coefficient evaluated based on (1) tends to be lower due to the effect of preferential trajectory.

The effect of nonlinear drag dependence is important for particles larger than the Kolmogorov scale (Mei, Adrian, and Hanratty[1]), while the preferential bias is dominant for small particles of size comparable to or smaller than the Kolmogorov scale (Wang and Maxey[2]). These two competing mechanisms can at least partially explain the large scatter of experimental data on the drag coefficient in turbulent flows shown in Fig. 1. Also plotted in the same figure for reference is the standard drag correlation applicable for the case of a stationary or steadily moving particle in a steady uniform ambient flow. The scatter in the data clearly illustrates the degree of disagreement as to the effect of turbulence. For example, in the moderate Reynolds number regime, the measurements of Uhlher and Sinclair,[3] Zarin and Nichols,[4] and Brucato *et al.*[5] indicated a substantial increase in the drag coefficient in a turbulent flow. The numerical study by Yusof[6] also illustrated a drag increase of nearly 40% in a freestream turbulence of 20% intensity. On the other hand, the results of Rudolff and Bachalo[7] tend to suggest a reduction in the drag coefficient due to ambient turbulence. In contrast, Warnica *et al.*[8] suggest that the drag on a spherical liquid drop is not significantly different from the standard drag. The experiments of Wu and Faeth[9,10] also suggest little influence of turbulence on the mean drag. The experiments of Torobin and Gauvin,[11,12] Clamen and Gauvin,[13] and Clift and Gauvin[14] pertain to particle Reynolds numbers greater than 1000, which is beyond the range of particulate flows. In this range an early transition to turbulence was observed in the boundary layer of a particle resulting in a sudden drop in the drag coefficient.

It should be noted that the effects of nonlinear drag dependence and trajectory bias can be easily accounted for, provided the drag coefficient is evaluated on an instantaneous basis using (1), with the instantaneous relative velocity between the particle and the surrounding fluid replacing the mean settling velocity V_T. The instantaneous drag coefficient thus evaluated may still differ from the standard drag, due to the effect of convective and temporal accelerations of the fluid and the particle, which give rise to the added-mass and the history forces. More important, the complex interactions between the various scales of turbulent flow and the particle can strongly influence the instantaneous drag. In the experimental results discussed above this inherent effect of turbulence is also present, apart from the effects of nonlinear drag dependence and trajectory bias. In this paper we focus on this inherent influence of turbulence in modifying the mean and instantaneous drag.

We consider the effects of turbulence on the forces on a stationary particle subjected to a stationary (frozen) isotropic turbulent flow which along with a uniform flow is applied as the freestream flow. The problem setup is very similar to that considered in the experiments of Wu and Faeth,[9,10] where a stationary particle was subjected to homogeneous turbulence. The range of parameters chosen in our study also matches with those of Wu and Faeth.[9,10] The present setup and parametric range are also similar to those considered by Mittal,[17] who performed numerical simulation of a stationary particle subjected to an oscillating uniform flow in lieu of a turbulent freestream.

The present methodology allows one to isolate the different mechanisms of drag modification by turbulence. First, the effect of the trajectory bias is avoided by considering a stationary particle. Second, the freestream turbulent flow to which the particle is subjected is computed from a separate simulation and hence is known *a priori*. As a result, the time history of the relative velocity between the particle and the ambient flow is known, and hence, the effects of nonlinear drag dependence can be precisely accounted for. The effect of the added-mass and history forces can also be accounted for from the precomputed turbulent field. The accuracy of the standard drag correlation in predicting the direct numerical simulation (DNS) drag can then be evaluated. Any discrepancy from the standard drag correlation can be interpreted as the inherent influence of turbulence.

In this paper, we present the DNS results on the mean and instantaneous drag and compare them with the predic-

tions based on the standard drag correlations such as the Schiller–Neumann formula (see Clift *et al.*[18]):

$$C_D = \frac{24}{\mathrm{Re}}(1 + 0.15\,\mathrm{Re}^{0.687}). \tag{2}$$

We consider the effects of varying the particle size and turbulence intensity, and as a result, the particle Reynolds number. The effect of including the added-mass and history forces with the Schiller–Neumann drag is also studied. The effect of different approximations for the fluid velocity seen by the particle is examined. The rms, mean squared difference, and cross-correlation of the DNS results and various predictions are presented. The DNS technique employed here is described in Sec. II. The results pertaining to the instantaneous drag, and the corresponding mean are given in Sec. III. Summary and conclusions are presented in Sec. IV.

II. METHODOLOGY

We consider interaction of a *single* spherical particle with isotropic turbulence. The turbulent field is a precomputed 256^3 DNS data in a cubic box obtained by Langford.[19] The field is periodic along all three directions and hence can be extended to any arbitrary large volume. The Kolmogorov length and velocity scales (η and v_k) are chosen as the reference length and velocity scales. The parameters that characterize the isotropic turbulence are as follows: root mean square of the turbulent velocity fluctuation (U_{rms}/v_k) is 6.5, box size (L/η) is 757.0, Taylor microscale (λ/η) is 25.2, and the microscale Reynolds number $\mathrm{Re}_\lambda = 164$.

An instantaneous realization of the isotropic field is considered and is represented by $\mathbf{U}(\mathbf{X})$, where ($\mathbf{X} = (X,Y,Z)$) is a fixed reference frame attached to the isotropic turbulent field. Thus the turbulent field is stationary (or, frozen in time). The turbulent field is superposed on a steady uniform freestream $\mathbf{V}$. Without loss of generality we assume that $\mathbf{V}$ is oriented along the X axis. In a reference frame (x,y,z) whose origin is fixed on to the center of a stationary particle the undisturbed ambient flow appears as $\mathbf{V} + \mathbf{U}(\mathbf{x} + \mathbf{X}_p(t))$, where $\mathbf{X}_p(t)$ is the instantaneous location of the center of the particle in the frame attached to the isotropic turbulent field and $\mathbf{x}$ is the location with respect to the particle. In other words, the turbulent field $\mathbf{U}(\mathbf{X})$ is swept past the stationary particle at the velocity $\mathbf{V}$. The computational domain attached to the particle is a spherical domain (r,θ,ϕ) whose outer radius R_O is 30 times the radius of the particle, a. The undisturbed ambient flow, as defined above, is specified at the inflow section of this outer boundary. A schematic view of the computation domain attached to the particle and the precomputed turbulent field is shown to scale in Fig. 2 for the case of $d/\eta = 10$. In general, the grid points of the spherical computational domain attached to the particle do not coincide with the grid points of the $(2\pi)^3$ cubic box in which the isotropic turbulent field is computed. Thus the turbulent velocity field $\mathbf{U}(\mathbf{X})$ has to be interpolated on to the outer boundary of the spherical domain. In order to retain spectral accuracy, the interpolation is done using Fourier summation.

It must be stressed here that we use an instantaneous three-dimensional field of precomputed isotropic turbulence to supply the turbulent inflow condition for the particle. Instead, an inflow could have been constructed as a uniform flow with superposition of a spectrum of modes with time-varying amplitudes to mimic the desired turbulence properties. Although somewhat computationally complicated, the application of the precomputed frozen isotropic box turbulence as the inflow condition provides a well-defined turbulent ambient flow which is characterized by a single parameter, the microscale Reynolds number.

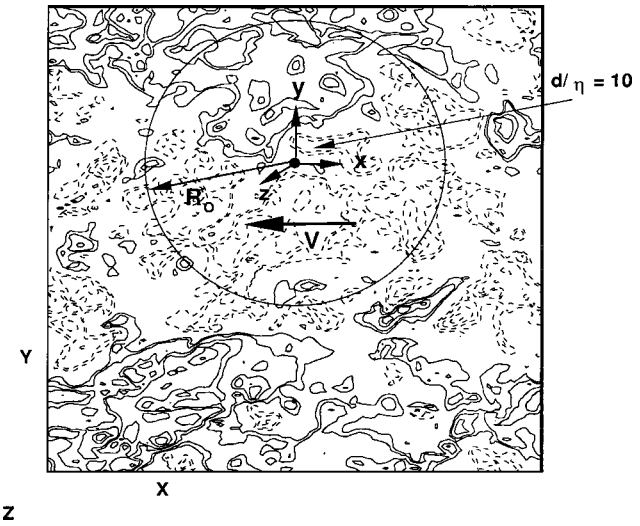

FIG. 2. Schematic of the particle–flow configuration. Drawn to the true scale, a particle of $d/\eta = 10$ is shown here. The large circle surrounding the particle represents the outer boundary of the spherical computational domain attached to the particle. The outer box represents the $(2\pi^3)$ box in which the isotropic turbulent flow is generated. Contours of one cross-stream velocity component scaled by $\langle|\mathbf{V}_r|\rangle$ are shown for $I = 0.1$.

In the spherical domain attached to the particle, the governing (continuity and Navier–Stokes) equations are solved by a direct numerical simulation. A Fourier–Chebyshev collocation scheme in spherical coordinates is used for the spatial discretization, and a two-step time-split scheme is used for the temporal discretization. Further details about the collocation method are given in Bagchi and Balachandar.[20] At the outflow boundary of the spherical domain, a nonreflecting boundary condition described by Mittal and Balachandar[21] is used. On the surface of the particle, no-slip and no-penetration conditions are satisfied. The distribution of the grid points is nonuniform: they are clustered near the surface of the particle and in the wake region. The grid resolution is chosen to satisfy two criteria: first, the size of the largest grid spacing in the spherical domain is less than that used to simulate the isotropic turbulent field, in order to guarantee resolution of the freestream turbulence. Second, the grid is adequate to resolve the thin shear layers and the wake structures generated by the particle. Typical grids used in the simulation have 141 points in the radial direction, 160 in the θ direction, and 128 in the ϕ direction.

The isotropic turbulence is periodic along all three directions. Thus, as the box of isotropic turbulence passes over the particle, the undisturbed ambient flow seen by the particle repeats after T units of time, where $T = L/|\mathbf{V}|$. The time scale of this long-term periodicity in the ambient flow is much

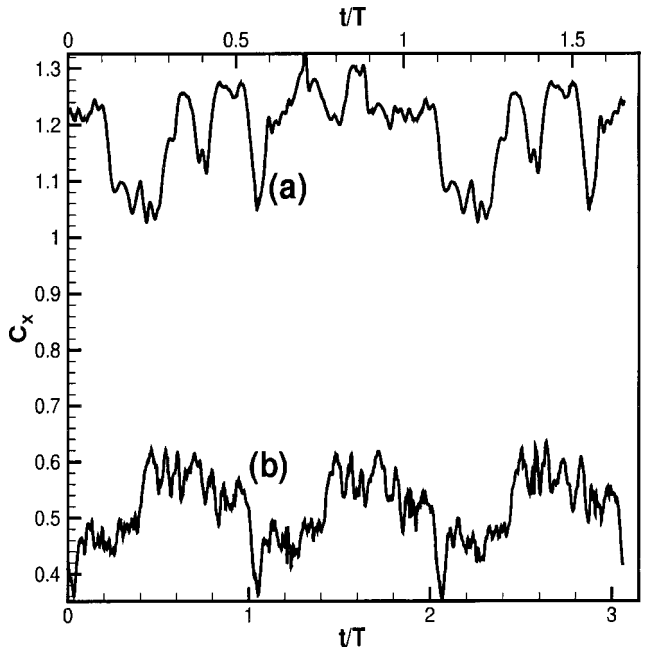

FIG. 3. Time history of drag response of the particle. The time periodic nature of the drag response with a period of T is shown. (a) $d/\eta = 1.5$, and (b) $d/\eta = 9.59$.

longer than the particle-induced disturbance flow time scale. In nondimensional terms, $T|\mathbf{V}|/d$, varied from about 1000 for the smallest particle to about 150 for the largest particle considered. The typical dimensionless time step $\Delta t|\mathbf{V}|/d$ used in the simulations is 0.0005. Thus the number of time steps for which time integration is performed is of the order of 10^6. This combined with the high grid resolution renders the computations very expensive. A typical computation requires about 20 000 CPU hours on Origin2000 supercomputer using 32 processors.

As the box of turbulence is repeatedly passed over the particle, the time history of lift and drag forces are monitored. At lower particle Reynolds numbers the wake simply responds to the ambient flow and the resulting force history repeats over time with period T. With increasing Reynolds number freestream turbulence only promotes and modulates the natural chaotic vortex shedding process. In this regime although the drag and lift histories are not strictly periodic over T, deviation from periodicity is observed to be small even for the largest particle considered. Figure 3 shows a time history of drag for the case $d/\eta = 1.5$ over $1.5T$, and for $d/\eta = 9.59$ over $3T$. The strict and approximate nature of time periodic behavior for the two different sizes can be observed. Time-averaged quantities to be reported here are computed by averaging over T or its integral multiple. Even for the largest particle, an average over $3T$ was observed to be adequate. The time-averaged mean quantities are denoted by the symbol $\langle\ \rangle$.

The parameters of this problem are the ratio of the particle diameter to the Kolmogorov scale of the isotropic turbulence d/η, the turbulence intensity defined as $\tilde{I} = U_{\rm rms}/|\langle \mathbf{V}_r \rangle|$, and the mean particle Reynolds number $\langle \mathrm{Re}_r \rangle = |\langle \mathbf{V}_r \rangle| d/\nu$, where $U_{\rm rms}$ is the rms of the fluctuations of the freestream turbulence, $\mathbf{V}_r = \mathbf{V} + \mathbf{U}(\mathbf{X}_p(t))$ is the instantaneous relative velocity between the particle and the undisturbed ambient flow measured at the center of the particle, and $\langle \mathbf{V}_r \rangle$ is the mean relative velocity obtained by time-averaging over T. Note that although the isotropic turbulent velocity averaged over the entire box is guaranteed to be zero, the mean turbulent velocity seen by the particle, $\langle \mathbf{U}(\mathbf{X}_p(t)) \rangle$, may be nonzero due to the limited volume sampled by the particle. The mean particle Reynolds number can be expressed in terms of the other two parameters as

$$\langle \mathrm{Re}_r \rangle = \frac{d/\eta}{\tilde{I}} \frac{U_{\rm rms}}{v_k}, \tag{3}$$

where v_k is the Kolmogorov velocity scale. For the isotropic turbulent flow considered here the velocity ratio $U_{\rm rms}/v_k = 6.5$. Here we discuss the results of six different simulations covering a range of parameter values given in Table I. The diameter of the particle is varied from about 1.5 to 10 times the Kolmogorov scale. Thus in all the cases considered the particle is bigger than the Kolmogorov scale but smaller than the Taylor microscale. The turbulence intensity is varied from 9% to 26%, and the resulting mean Reynolds number varies from about 60 to 610. We also define a modified freestream intensity as $I = U_{\rm rms}/|\mathbf{V}|$, which is also given in the table. The parametric range chosen for the present study is in reasonable agreement with many previous works that are aimed at studying particle–turbulence interaction (see Table II). A variety of flows ranging from homogeneous turbulence to pipe flow, channel flow, and jets have been studied. In many of these studies the particle size ranges from about the Kolmogorov scale up to the Taylor microscale (Tsuji *et al.*,[22] Wu and Faeth,[9,10] Mizukami *et al.*,[23] Parthasarathy and Faeth,[24] Yusof[6]). In many of these studies the focus has been the interaction of turbulence with a distribution of large number of particles. Of particular relevance to the present study is the experimental work of Wu and Faeth,[9,10] who considered the interaction of a single particle subjected to homogeneous turbulence.

TABLE I. Parametric range of the present study. η = Kolmogorov scale; λ = Taylor microscale; Λ = integral scale.

Case	d/η	d/λ	d/Λ	$\tilde{I} = U_{\rm rms}/\langle \lvert \mathbf{V}_r \rvert \rangle$	$I = U_{\rm rms}/\lvert \mathbf{V} \rvert$	$\langle \mathrm{Re}_r \rangle$
1	1.53	0.061	0.003	0.093	0.1	107
2	1.53	0.061	0.003	0.171	0.2	58
3	3.84	0.152	0.008	0.096	0.1	261
4	3.84	0.152	0.008	0.219	0.25	114
5	9.59	0.381	0.019	0.103	0.1	609
6	9.59	0.381	0.019	0.259	0.25	241

Validation. The simulation technique described above has been used previously to address few other problems on shear, straining, and vortical flow past a particle (Bagchi and Balachandar).[20,28–30] Extensive tests on the accuracy of the simulation technique have been performed and documented.[20,31] Results on spectral decay at various points within the computational domain, sensitivity to grid resolution, and detailed comparison with prior simulations and ex-

TABLE II. Some experimental works on particle-flow interaction and their parametric range. Here $^+$ indicates that the number is τ_p/τ_f, the ratio of particle response time to fluid time scale.

Experiments	d/η	d/λ	I	$\langle \mathrm{Re}_r \rangle$
Pipe flow[a]	2–60	0.13–2	0.05–0.15	
Homogeneous turbulence[b]	1.2–12	0.13–2	0.04–0.07	135–1560
Homogeneous turbulence[c]	1.2–8		0.02–0.08	38–545
Particle-laden jet[d]			0.05–0.15	100–750
Particle-laden jet[e]	$7-29^+$			
Channel flow[f]	$0.57-3^+$		0.05–0.2	5–20
Stirred vessel[g]	1.5–35			0.2–40
Isotropic (frozen)[h]	5.2–14.3		0.03–0.19	100

[a]Tsuji *et al.* (Ref. 22).
[b]Wu and Faeth (Refs. 9 and 10).
[c]Parthasarathy and Faeth (Ref. 24).
[d]Tsuji *et al.* (Ref. 25).
[e]Longmire and Eaton (Ref. 26).
[f]Kulick *et al.* (Ref. 27).
[g]Brucato *et al.* (Ref. 5).
[h]Yusof (Ref. 6). Note that Yusof's work is a numerical investigation.

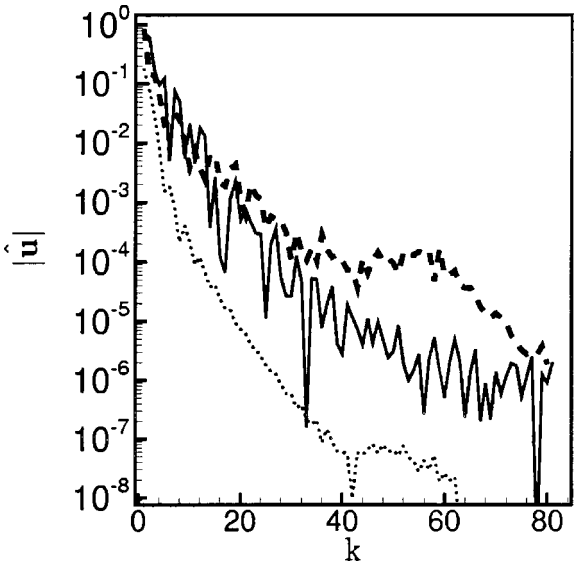

FIG. 4. Instantaneous velocity spectra along three coordinate directions for the case $d/\eta=9.59$, $I=0.1$. Radial spectra (—); θ spectra (---); ϕ spectra ($\cdots$).

periments have been discussed. For example, a documentation on the accuracy of the drag coefficient in uniform flow is given in Table III. The drag coefficient C_D, obtained from the present simulations, agrees well with the experimental correlation of Clift *et al.*[18] Good agreement is also observed with the numerical results obtained by Mittal[32] and Magnaudet *et al.*[33] The effect of domain size was investigated by doubling the size of the computational domain to 60 times the particle radius. The mean drag coefficient obtained for the case of a linear shear flow varied by less than 0.02% and the corresponding change in mean lift was even smaller. The larger domain employed a proportionately increased grid resolution and thus the difference corresponds to the placement of the outer computational boundary. A domain size of 30 particle radius corresponds to a blockage of about 0.1% and thus the small influence can be expected.

In the context of spectral methods used here, the adequacy of grid resolution can be investigated in terms of the decay of the velocity spectra with respect to wave number. The spectra of velocity at a point in the shear layer for a turbulent flow at $\langle \mathrm{Re}_r \rangle=609$, $d/\eta=9.59$, $I=0.1$ along all three directions is shown in Fig. 4. A decay of six to nine orders of magnitude is observed in the radial, tangential, and azimuthal spectra. Similar investigation of spectral decay at other critical points within the flow suggests adequate resolution even for the highest Re considered here. Similar checks on the adequacy of resolution have been performed for all simulations reported here.

TABLE III. Comparison of present simulations with previous experimental and numerical results for uniform flow past a particle.

Re	Present simulations C_D	Previous results C_D
10	4.30	4.32[a]
50	1.57	1.54,[b] 1.57[c]
100	1.09	1.09,[b] 1.09[c]
200	0.77	0.80,[b] 0.765[a]
250	0.70	0.73,[b] 0.68[c]
350	0.62	0.64,[b] 0.62[c]
500	0.56	0.56[b]

[a]Magnaudet *et al.* (Ref. 33).
[b]Clift *et al.* (Ref. 18).
[c]Mittal (Ref. 32).

III. EFFECT OF TURBULENCE ON DRAG

A. Mean drag

The instantaneous force on the particle is computed in the DNS by integrating the pressure and shear stresses on the surface of the particle as

$$\mathbf{F}(t)=\int_S [-p\mathbf{e}_r+\tau_{r\theta}\mathbf{e}_\theta+\tau_{r\phi}\mathbf{e}_\phi]dS. \tag{4}$$

The component of this force along the direction of the instantaneous relative velocity $\mathbf{V}_r$ is the instantaneous drag force, F_D, and the normal component is the instantaneous lift force, F_L. Note that the instantaneous relative velocity and hence the drag force constantly changes direction, although they are oriented nearly along the x axis since $U_{\mathrm{rms}}/|\mathbf{V}|$ considered here is at the most 25%. The mean drag force from the DNS data is evaluated as

$$\langle F_D \rangle=\langle |\mathbf{F}(t)\cdot\hat{\mathbf{V}}_r| \rangle, \tag{5}$$

where $\hat{\mathbf{V}}_r$ is the unit vector along the relative velocity. The dimensionless mean drag coefficient is computed by

$$C_D=\frac{\langle F_D \rangle}{\frac{1}{2}\rho_f \pi (d/2)^2 \langle |\mathbf{V}_r| \rangle^2}, \tag{6}$$

where ρ_f is the density of the fluid. The DNS result of the mean drag coefficient is presented in Fig. 1, along with the past experimental results. The present DNS results compare reasonably well with the standard drag curve implying that

TABLE IV. Mean drag.

$\langle \mathrm{Re}_r \rangle$	d/η	$I=U_{\mathrm{rms}}/\lvert\mathbf{V}\rvert$	DNS drag	Estimate 1	Estimate 2	Estimate 3
107	1.5	0.1	1.07	1.08	1.06	0.96
58	1.5	0.2	1.53	1.52	1.43	1.20
261	3.8	0.1	0.71	0.73	0.72	0.68
114	3.8	0.25	1.03	1.10	1.04	0.89
609	9.6	0.1	0.54	0.53	0.52	0.55
241	9.6	0.25	0.68	0.80	0.75	0.84

the freestream turbulence does not have a substantial effect on the mean drag at least over the range of Reynolds numbers considered.

A more quantitative comparison is presented in Table IV, where the DNS result is compared with two different estimates based on the standard drag correlation by Schiller and Neumann (Clift *et al.*[18]) as given in (2). The first estimate is obtained by applying the Schiller–Neumann formula to compute the instantaneous drag from the time-dependent relative velocity $\mathbf{V}_r$ and Reynolds number $\mathrm{Re}_r(t)=|\mathbf{V}_r|d/\nu$, and then averaging over time T. The second estimate is based on the time-averaged relative velocity $\langle \mathbf{V}_r \rangle$ and Reynolds number $\langle \mathrm{Re}_r(t) \rangle$ applied directly to the Schiller–Neumann formula (2).[34] These estimates can be expressed as

$$\text{Estimate 1:} \quad \langle F_D \rangle_1 = \langle \tfrac{1}{2}\rho_f \pi (d/2)^2 C_D(\mathrm{Re}_r)|\mathbf{V}_r|^2 \rangle, \quad (7)$$

$$\text{Estimate 2:} \quad \langle F_D \rangle_2 = \tfrac{1}{2}\rho_f \pi (d/2)^2 C_D(\langle \mathrm{Re}_r \rangle)|\langle \mathbf{V}_r \rangle|^2, \quad (8)$$

where

$$C_D(\mathrm{Re}_r) = \frac{24}{\mathrm{Re}_r}[1+0.15\,\mathrm{Re}_r^{0.687}], \quad (9)$$

$$C_D(\langle \mathrm{Re}_r \rangle) = \frac{24}{\langle \mathrm{Re}_r \rangle}[1+0.15\langle \mathrm{Re}_r \rangle^{0.687}]. \quad (10)$$

The difference between the above two estimates highlights the effect of nonlinear drag dependence. It can be seen from Table IV that both of these estimates differ from the DNS result by at most 17%, but for most cases the difference is less than 8%. The difference does not appear to have any systematic dependence on the Reynolds number or turbulence intensity. In some cases the difference is positive and in others it is negative.

The estimate 1 differs from 2 by less than 6%, which implies that the effect of nonlinear drag dependence is minimal in the parametric range of the present simulations. The fractional difference between the two estimates can be expressed as

$$\frac{|\langle F_D \rangle|_1 - |\langle F_D \rangle|_2}{|\langle F_D \rangle|_2} \approx \frac{0.58\alpha\langle \epsilon^2 \rangle}{1+\alpha}, \quad (11)$$

where $\alpha = 0.15\langle \mathrm{Re}_r \rangle^{0.687}$, and the small parameter $\epsilon = (|\mathbf{V}_r| - |\langle \mathbf{V}_r \rangle|)/|\langle \mathbf{V}_r \rangle|$ measures the level of fluctuation in the freestream turbulence. By definition, $\langle \epsilon \rangle = 0$, and $I^2 = U_{\mathrm{rms}}^2/|\mathbf{V}|^2$ provides a reasonable measure of $\langle \epsilon^2 \rangle$. The effect of nonlinear drag dependence is thus likely to be significant only at large Reynolds numbers, when α is large, and when the level of freestream fluctuation is quite strong. Based on the above equation the effect of nonlinearity for the different cases considered here can be estimated to be weak, only ranging from about 0.4% to 3.3%.

It is thus clear that freestream turbulence, at least over the range of parameters considered, has no systematic effect on the time-averaged mean drag force. Therefore, the use of the standard drag correlation, based on the instantaneous or mean relative velocity, will result in a reasonably accurate prediction of the mean drag force. However, as will be discussed next, the accuracy of prediction of the instantaneous drag force will depend on both the size of the particle and the turbulence intensity.

The mean drag is however dependent on the definition of the mean fluid velocity seen by the particle. The mean fluid velocity obtained by averaging over the entire volume of fluid can result in a significantly different estimate of the mean drag if the particle does not sample the entire volume. For example, in the present simulations, the mean velocity of the entire cubic box of turbulence swept past the particle is $\mathbf{V}$. Similar to (7) and (8), an estimate of the mean drag based on $\mathbf{V}$ can be obtained as

$$\text{Estimate 3:} \quad \langle F_D \rangle_3 = \tfrac{1}{2}\rho_f \pi (d/2)^2 C_D(\mathrm{Re}_p)|\mathbf{V}|^2$$

where

$$\mathrm{Re}_p = \frac{|\mathbf{V}|d}{\nu}, \quad (12)$$

which is also presented in Table IV. A discrepancy as high as 22% for case 2 ($d/\eta=1.5, I=0.2, \langle \mathrm{Re}_r \rangle = 107$) is observed with respect to the DNS drag. The difference between this estimate and the one given in (8) is due to the difference in the definition of the mean fluid velocity seen by the particle. If we take the difference to be represented by a small parameter $\delta = (\mathbf{V} - |\langle \mathbf{V}_r \rangle|)/|\langle \mathbf{V}_r \rangle|$, then the fractional difference between the two estimates can be expressed as

$$\frac{|\langle F_D \rangle|_3 - |\langle F_D \rangle|_2}{|\langle F_D \rangle|_2} \approx \frac{\delta(1+1.687\alpha)}{1+\alpha}. \quad (13)$$

Any uncertainty in the mean fluid velocity seen by the particle will influence the mean drag estimation linearly, and the relative turbulence intensity, I, provides a measure for the possible uncertainty in the mean fluid velocity. Thus, unlike the effect of nonlinear drag dependence where the influence of perturbation is quadratic, here it is linear. Also note that for the same level of uncertainty, the error will be 68.7% larger at higher Reynolds number than in the Stokes limit. Although the present simulations consider only a stationary particle, the above results suggest the potential importance of preferential particle trajectory on the mean drag, if the particle was allowed to fall freely through isotropic turbulence, as in some experiments.

B. Instantaneous drag

The time history of the forces on the particle is shown in Figs. 5 and 6. Three different cases of the particle diameter $d/\eta = 1.5$, 3.8, and 9.6 are considered, while the turbulence intensity, as $I = U_{\mathrm{rms}}/|\mathbf{V}|$, is fixed at 0.1. Since the instantaneous relative velocity and hence the drag force constantly

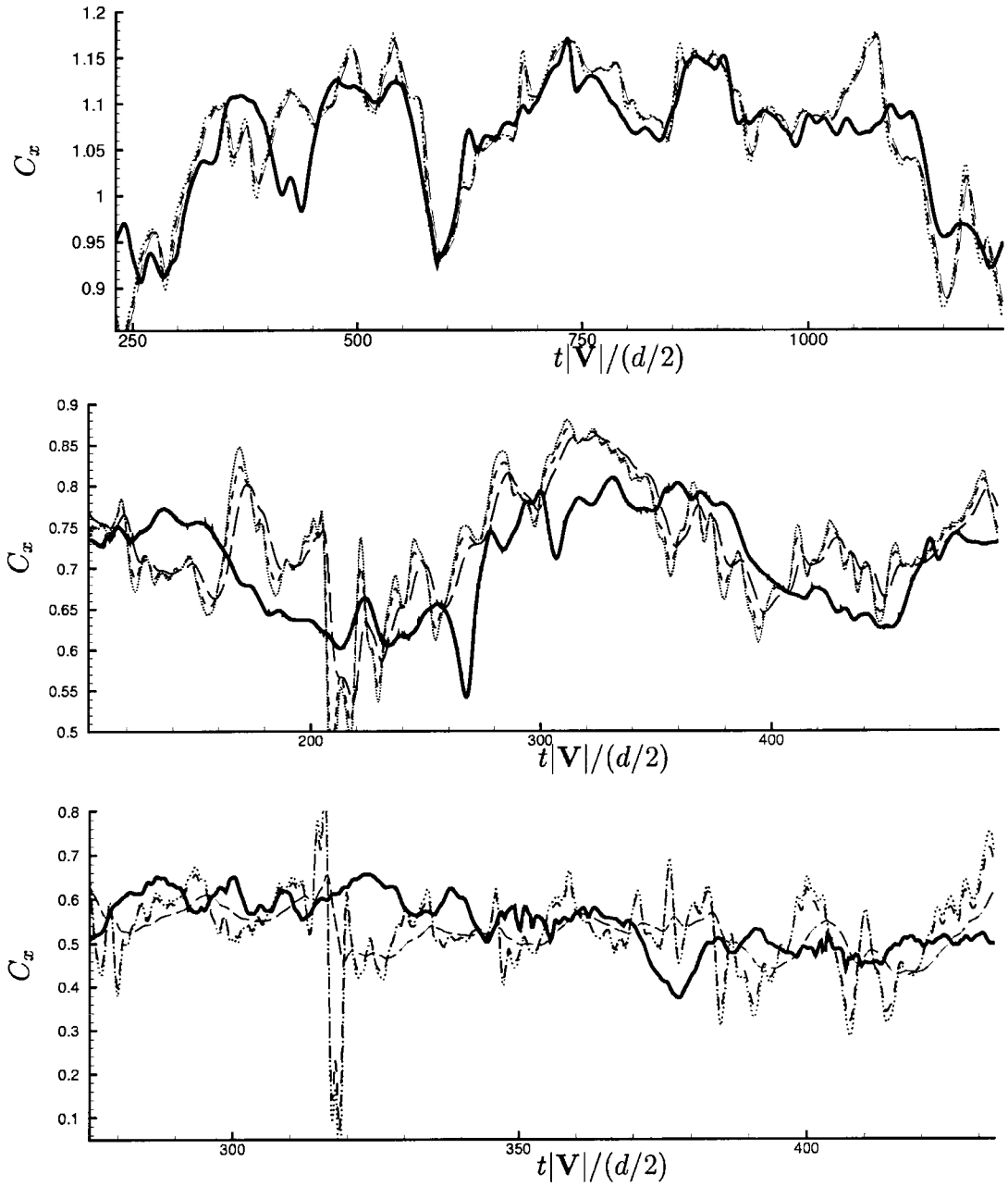

FIG. 5. Time history of C_x. Top: case 1 ($d/\eta=1.5, I=0.1, \langle \mathrm{Re}_r \rangle = 107$), middle: case 3 ($d/\eta=3.8, I=0.1, \langle \mathrm{Re}_r \rangle = 261$), bottom: case 5 ($d/\eta=9.6, I=0.1, \langle \mathrm{Re}_r \rangle = 609$). (—) DNS result (thick line); (– – –) Schiller–Neumann law (2); (---) plus the inertial force; (···) plus the history force (14).

change direction it is convenient to write the net force in nondimensional form as $\mathbf{C_F} = C_x\mathbf{e}_x + C_y\mathbf{e}_y + C_z\mathbf{e}_z$, where C_x, C_y, and C_z are the force coefficients in the x, y, and z directions, respectively. The coefficients C_x and C_y are shown in Figs. 5 and 6, respectively. Note that C_y and C_z are primarily determined by the lift force and are similar in nature and smaller in magnitude than C_x which mostly represents the drag force.

The DNS results of C_x and C_y are compared against the estimates using the Schiller–Neumann law based on the instantaneous relative velocity $\mathbf{V}_r$. Also presented in Figs. 5 and 6 are the estimates that include the inertial (added-mass and pressure gradient) force and the history force, which are also evaluated based on the undisturbed ambient flow at the particle center. For the present case of a stationary particle these additional contributions can be written in dimensional form as

$$\mathbf{F}_{\text{inertial}} = \tfrac{3}{2} m_f \mathbf{V}\cdot\nabla\mathbf{U},$$
$$\mathbf{F}_{\text{history}} = 3d\pi\mu \int_{-\infty}^{t} K(t,\tau)\mathbf{V}\cdot\nabla\mathbf{U}\, d\tau, \tag{14}$$

where m_f is the mass of the fluid that can occupy the volume of the particle, K is the history kernel, τ is time, and μ is fluid viscosity. The expressions for the inertial and history forces given above correspond to the unsteady undisturbed ambient flow seen by the particle as the isotropic turbulence sweeps past the particle at velocity $\mathbf{V}$. For the history kernel $K(t,\tau)$ the expression given by Mei and Adrian[35] appropriate for moderate Reynolds number is used.

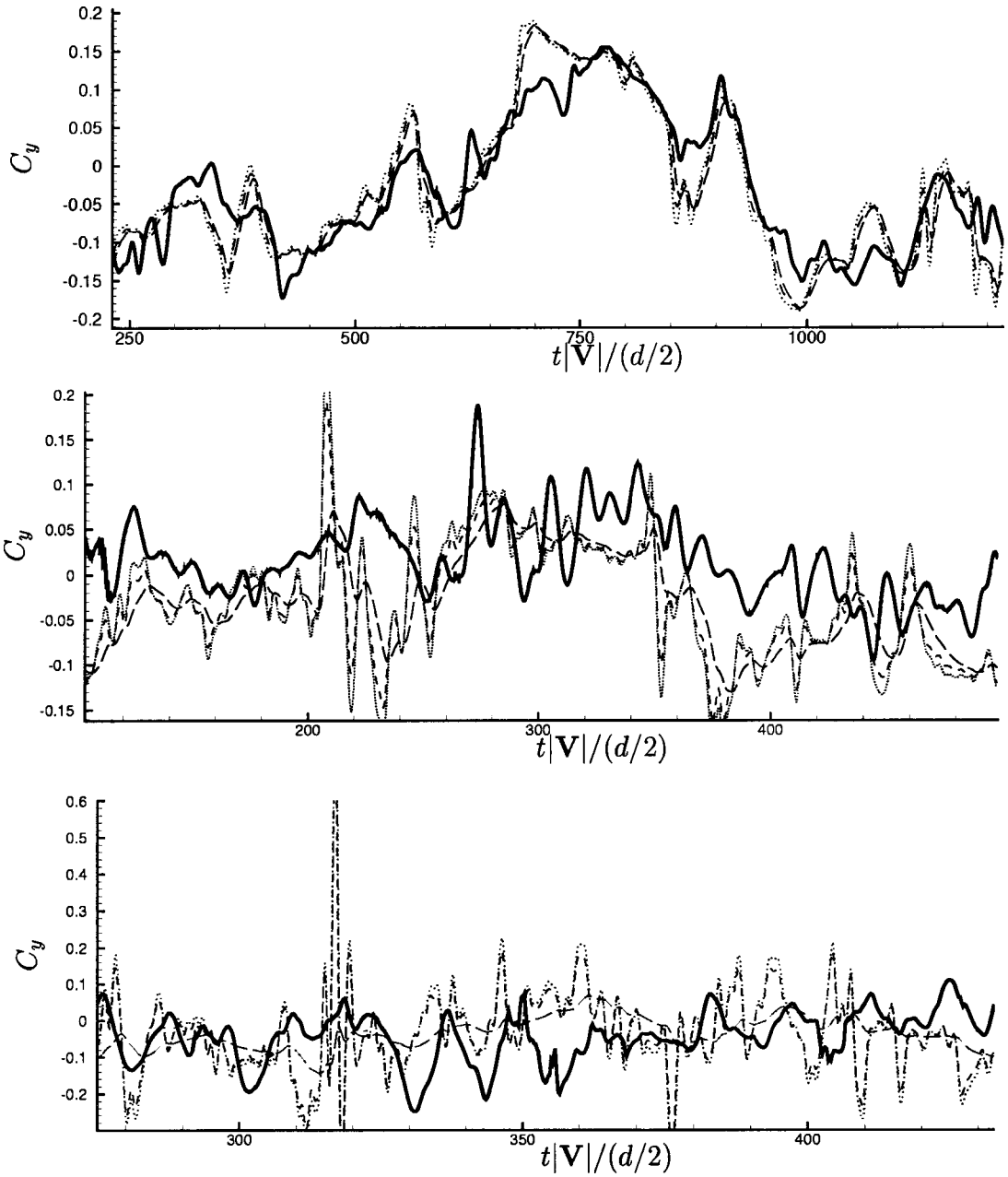

FIG. 6. Time history of C_y. Top: case 1 ($d/\eta=1.5, I=0.1, \langle \mathrm{Re}_r \rangle = 107$), middle: case 3 ($d/\eta=3.8, I=0.1, \langle \mathrm{Re}_r \rangle = 261$), bottom: case 5 ($d/\eta=9.6, I=0.1, \langle \mathrm{Re}_r \rangle = 609$). Symbols have the same meaning as in Fig. 5.

It should be emphasized that here the particle is stationary (non-accelerating) and the added-mass and Basset history forces are due to acceleration of the ambient flow seen by the stationary particle, given by $\mathbf{V}\cdot\nabla\mathbf{U}$. Since the particle is stationary, particle density, or mass of the particle, is not of relevance in the present simulations. As a result the standard argument that the added-mass and Basset history forces are negligible for large particle-to-fluid density ratio does not apply. In fact, scaling arguments[30] show that added-mass and Basset forces due to fluid acceleration are dependent only on particle Reynolds number and lengthscale ratio. As will be seen below the added-mass force evaluated based on (14) is of significant value, especially for the largest particle considered.

The detailed time-dependence of the drag and lift forces as obtained from the DNS is not precisely reproduced by any of the estimates. For the smallest particle considered (case 1: $d/\eta=1.5$, $I=0.1$, $\langle \mathrm{Re}_r \rangle = 107$), the slow variations in the DNS force are predicted well by the Schiller–Neumann law, whereas the high-frequency fluctuations are not captured. As the particle diameter increases to $d/\eta=9.59$, the slow variations are no longer accurately predicted by the Schiller–Neumann law. Contribution from the added-mass is quite small for the smallest particle (case 1), but substantially high for the larger particle. Nevertheless, the inclusion of the added-mass force appears to only worsen the prediction by introducing high frequency oscillations (Figs. 5 and 6). Contribution from the history force, as evaluated by the integral given above, is negligible in all the above cases considered.

The Reynolds number for the $d/\eta=9.6$, $I=0.1$ case is

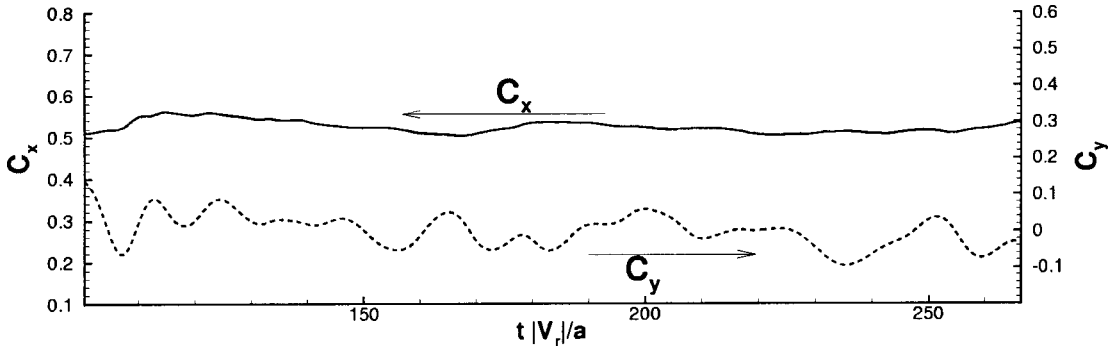

FIG. 7. Time history of C_x and C_y for uniform flow corresponding to case 5 ($\langle \mathrm{Re}_r \rangle = 609$).

about 609 and therefore the flow in the wake of the particle undergoes a natural vortex shedding process. As a result the drag and lift forces for this case are time-dependent even in a non-turbulent uniform ambient flow. The time history of C_x and C_y corresponding to the uniform ambient flow at $\langle \mathrm{Re}_r \rangle = 609$ is shown in Fig. 7. It is interesting to note that the level of fluctuations in C_x in the uniform flow is much lower than that in the turbulent flow. In comparison, the level of fluctuations in C_y is comparable to the turbulent flow, although some high frequency oscillations can be observed in the case of turbulent flow. Note that in a uniform flow the lift force is generated only due to the vortex shedding process. Freestream turbulence can promote an early onset of vortex shedding. But once the vortex shedding process is established, owing to its absolutely unstable nature, it is only weakly influenced by the freestream turbulence and correspondingly the lift force fluctuates primarily in response to the shedding process with only a weak influence from the freestream turbulence. The drag force, on the other hand, shows substantially enhanced fluctuations in the turbulent flow compared to the uniform flow.

C. Spectra

The spectra of the time-dependent forces corresponding to Figs. 5 and 6 are shown in Fig. 8. Here the turbulence intensity is maintained at $I = 0.1$, while d/η increases from 1.5 to 9.6. The spectra are obtained by taking the Fourier transform of the drag and lift forces shown in Figs. 5 and 6. The horizontal axis in Fig. 8 represents the Strouhal number $\mathrm{St} = fd/|\mathbf{V}|$, where f is the frequency of oscillation in the drag and lift forces. The smallest nonzero St corresponds to the period T over which the isotropic box of turbulence passes over the particle ($\Delta \mathrm{St} = d/(T|\mathbf{V}|)$). The zero frequency (not shown in the figure) corresponds to the mean drag and lift forces as given in Table IV. The spectra of C_x and C_y predicted by the Schiller–Neumann law applied on an instantaneous basis are also shown along with those of the DNS data. Note that the spectra appear jagged since only one realization of the freestream turbulent flow is considered. Further, the same region of fluid is passed over the particle in every pass. Of course, if many realizations are used, or if different regions of flow are passed over the particle each time, the spectra will show a smooth decay. The figures support the observation made earlier that the low frequency component of the DNS data for the smallest particle is well captured by the Schiller–Neumann law applied on an instantaneous basis. At higher frequencies the difference between the DNS data and the Schiller–Neumann prediction increases. For the larger particles, significant difference can be observed in C_x and C_y even at the lowest frequencies. The spectra of C_y (and also C_z) are likely to be influenced the most by the fluctuating lift force, since the flow is dominantly oriented along the x direction.

For the smallest particle the Reynolds number is sufficiently low and therefore vortex shedding is not expected. The wake only oscillates in response to the freestream turbulence. Thus the spectra of DNS results nearly follow those predicted by the Schiller–Neumann law. For the intermediate particle of size $d/\eta = 3.8$, the Reynolds number $\langle \mathrm{Re}_r \rangle = 261$,

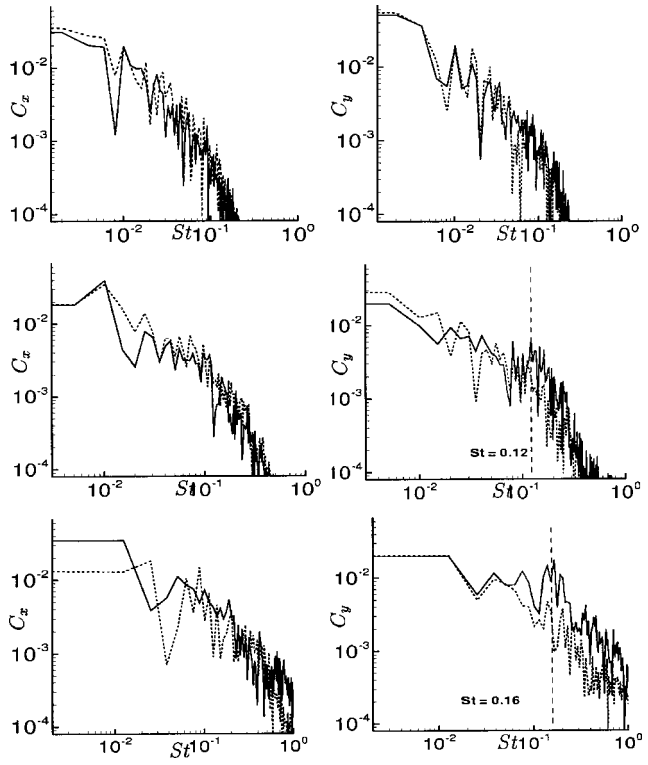

FIG. 8. Spectra of C_x (left panel) and C_y (right panel). Top: $d/\eta = 1.5$, $\langle \mathrm{Re}_r \rangle = 107$, middle: $d/\eta = 3.8$, $\langle \mathrm{Re}_r \rangle = 261$, bottom: $d/\eta = 9.6$, $\langle \mathrm{Re}_r \rangle = 609$. For all cases, $I = U_{\mathrm{rms}}/|\mathbf{V}| = 0.1$. (—) DNS result; (···) Schiller–Neumann.

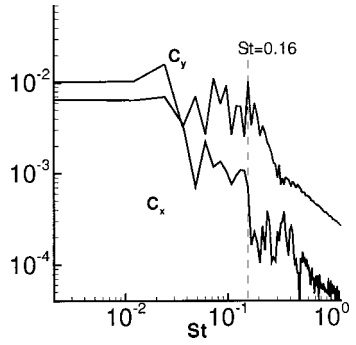

FIG. 9. Spectra of C_x and C_y for uniform flow corresponding to case 5 ($\langle \mathrm{Re}_r \rangle = 609$).

and in a turbulence-free uniform flow there is no vortex shedding at this Reynolds number. However, the presence of freestream turbulence destabilizes the wake and results in an early initiation of vortex shedding. An extrapolation of the Strouhal number versus Reynolds number curve yields an approximate Strouhal number of about 0.12 at $\langle \mathrm{Re}_r \rangle = 261$ (Mittal[17]). Figure 8 shows a modest local peak in the spectra of C_y around this St. For the case of $d/\eta = 9.6$, $I = 0.1$, $\langle \mathrm{Re}_r \rangle = 609$, the spectra of C_y shows a local peak around St $= 0.16$. The spectra for the uniform flow at this Reynolds number is shown in Fig. 9, which also shows a local peak in C_y around St $= 0.16$. This is consistent with the previous observation that the lift is not substantially influenced by the freestream turbulence for the largest particle. Also note that the amplitude of high-frequency oscillations is higher in C_y than in C_x for both the uniform and turbulent flows for the largest particle.

D. rms and cross-correlation

The root-mean-square (rms) of the fluctuations in C_x, C_y, and C_z is shown in Fig. 10 as a function of the particle size for $I = 0.1$. The rms fluctuations for the force coefficients are defined as

$$C_x' = \sqrt{\langle (C_x - \langle C_x \rangle)^2 \rangle}, \quad C_y' = \sqrt{\langle (C_y - \langle C_y \rangle)^2 \rangle}, \quad C_z' = \sqrt{\langle (C_z - \langle C_z \rangle)^2 \rangle}. \tag{15}$$

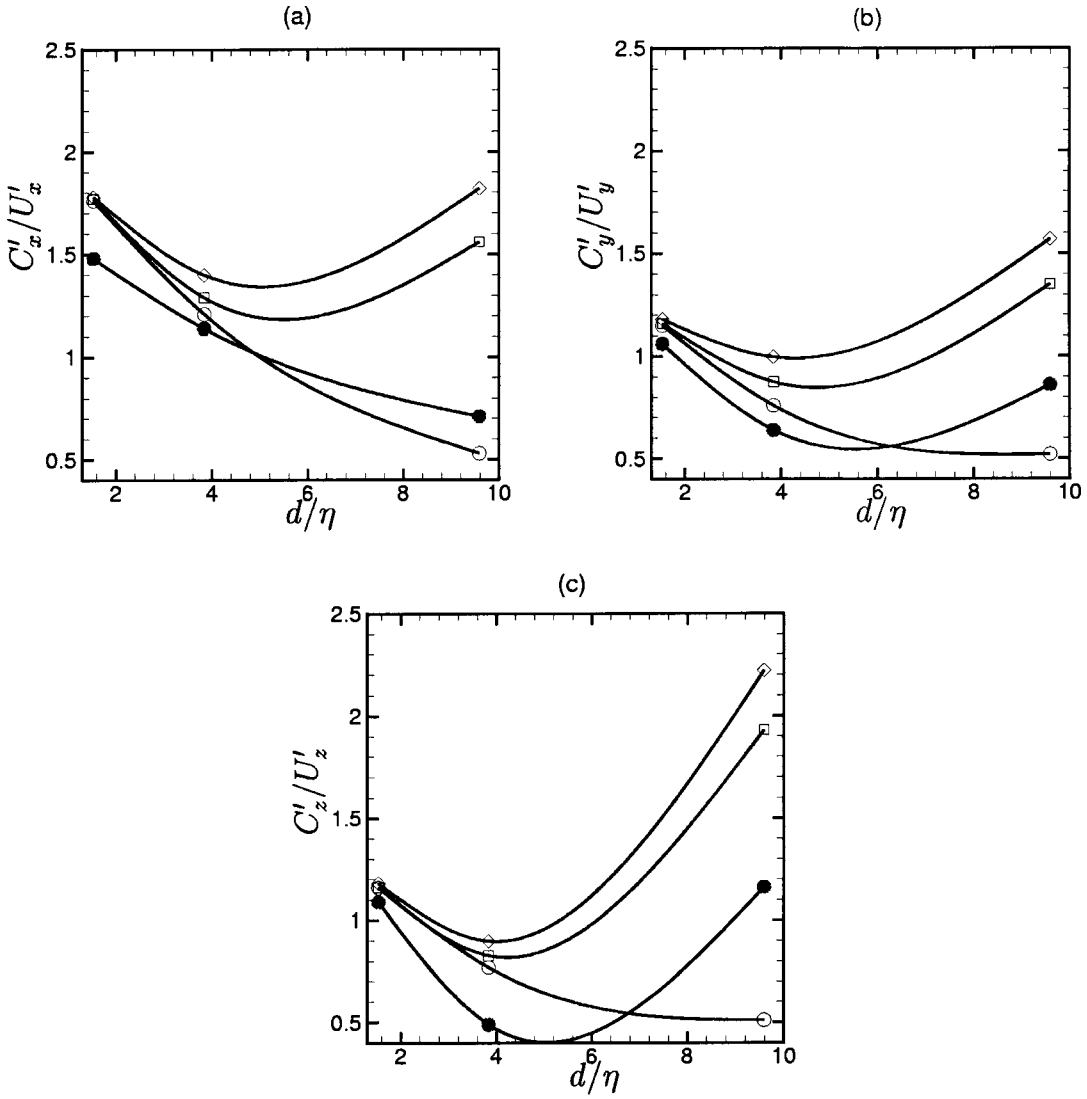

FIG. 10. rms of fluctuations in the force for $I = 0.1$. (●) DNS (○) Schiller–Neumann law (2), (□) plus the inertial force, (◇) plus the history force.

In the figure these quantities are scaled by the corresponding freestream velocity fluctuations obtained as

$$U_x' = \sqrt{\langle (U_x - \langle U_x \rangle)^2 \rangle}, \quad U_y' = \sqrt{\langle (U_y - \langle U_y \rangle)^2 \rangle}, \quad U_z' = \sqrt{\langle (U_z - \langle U_z \rangle)^2 \rangle}, \tag{16}$$

where $\mathbf{U} = \mathbf{U}(\mathbf{X}_p(t))$ is the instantaneous undisturbed turbulent velocity measured at the center of the particle. The DNS result is compared with the predictions based on the Schiller–Neumann law and with those including the added-mass and the history forces given by (14). For all particle sizes, the prediction using the Schiller–Neumann law appears to be the closest to the DNS result. The effect of including the inertial and history forces is negligible for the smallest particle, and substantial for the largest one. Note that for the smallest particle, the prediction is better for the cross-stream components C_y' and C_z' than for the streamwise component C_x'. For the largest particle (case 5), the reverse is the case. This is because for the smallest particle the cross-stream forces in a uniform flow are zero. In a turbulent flow these forces are entirely induced by the freestream turbulence and hence they tend to closely follow the freestream oscillation. For the largest particle, on the other hand, in an otherwise steady uniform flow unsteady vortex shedding occurs in the wake which generates the fluctuating cross-stream forces.

TABLE V. Cross correlation between DNS force and the ambient turbulent velocity.

Case	d/η	$I = U_{\text{rms}}/\lvert\mathbf{V}\rvert$	$\langle \text{Re}_r \rangle$	C_x and U_x	C_y and U_y	C_z and U_z
1	1.5	0.1	107	0.852	0.915	0.928
2	1.5	0.2	58	0.842	0.917	0.935
3	3.8	0.1	261	0.634	0.536	0.628
4	3.8	0.25	114	0.488	0.079	0.081
5	9.6	0.1	609	0.258	0.002	0.086
6	9.6	0.25	241	0.13	−0.25	0.079

The unsteady vortex shedding persists in the turbulent ambient flow as well resulting in a significant enhancement in the fluctuation of the cross-stream forces.

In Fig. 10 it can be observed that for the smallest particle of $d/\eta = 1.5$, the DNS results show that $C_y'/U_y' \approx C_z'/U_z'$. Thus the fluctuations are axisymmetric about the mean wake centerline, as the wake is dominated by the freestream isotropic turbulence. The axisymmetry is however lost at higher $\langle \text{Re}_r \rangle$, and C_y'/U_y' considerably differs from C_z'/U_z'. In a uniform ambient flow, at $\langle \text{Re}_r \rangle = 609$, there is an approximate plane of symmetry in the wake and the lift force lies on this plane. In a turbulent flow, the shedding process varies with time, and a plane of symmetry is not observed. However, a complete axisymmetry about the wake centerline is not achieved, and hence C_y'/U_y' and C_z'/U_z' are not the same.

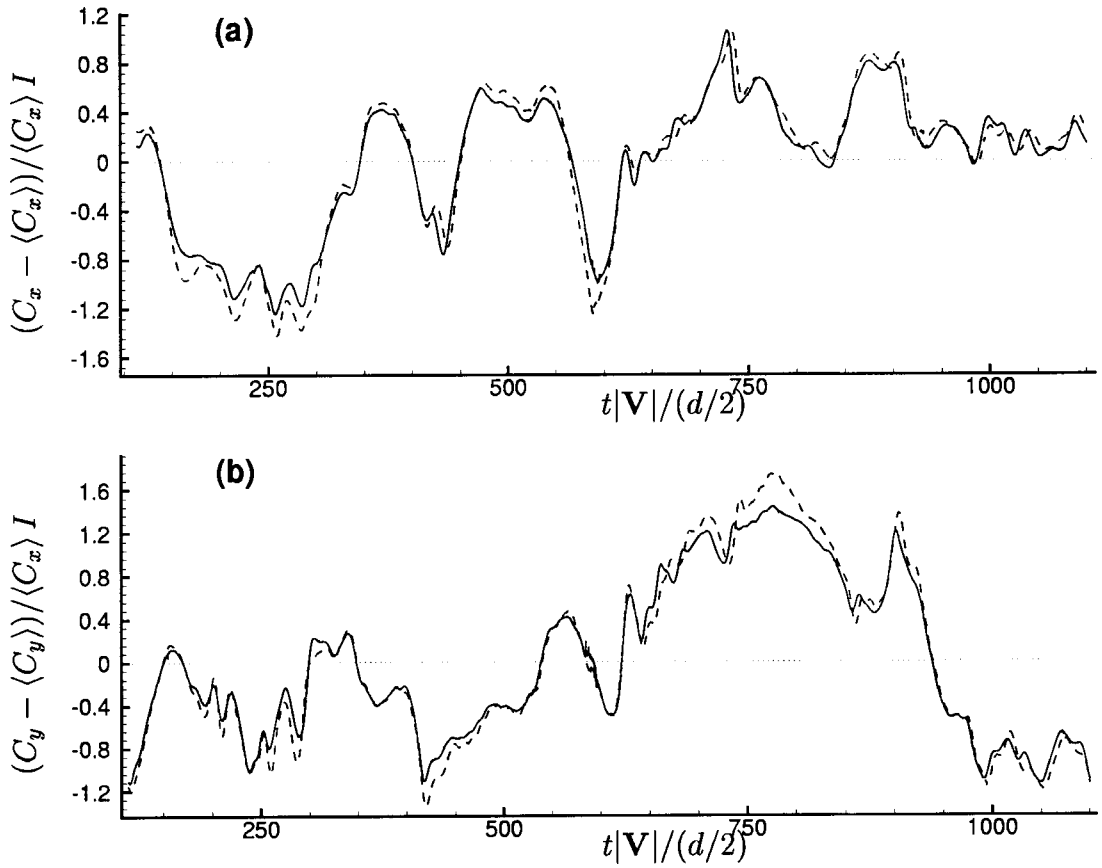

FIG. 11. Effect of increasing freestream turbulence intensity while the particle size is fixed at $d/\eta = 1.5$. (—) $I = 0.2$; (---) $I = 0.1$. (a) $(C_x - \langle C_x \rangle)/\langle C_x \rangle I$, (b) $(C_y - \langle C_y \rangle)/\langle C_x \rangle I$.

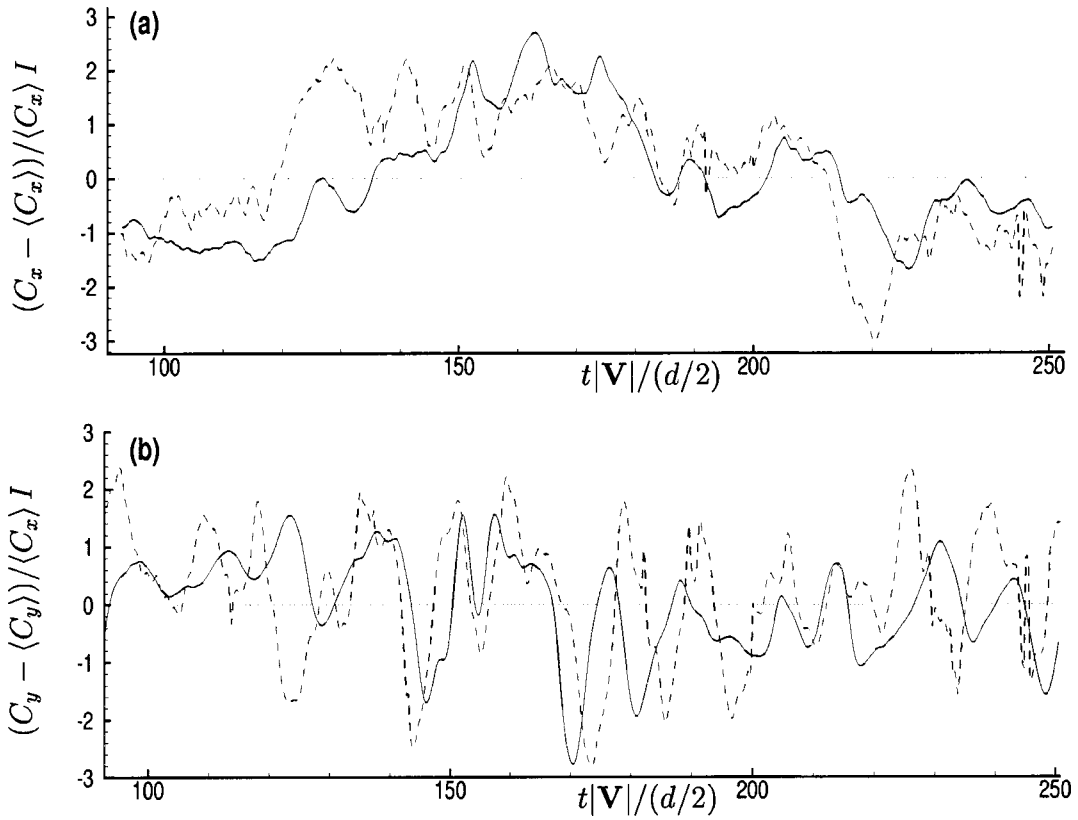

FIG. 12. Effect of increasing freestream turbulence intensity while the particle size is fixed at $d/\eta = 9.6$. (—) $I = 0.25$; (---) $I = 0.1$. (a) $(C_x - \langle C_x \rangle)/\langle C_x \rangle I$, (b) $(C_y - \langle C_y \rangle)/\langle C_x \rangle I$.

It is also interesting to compare the rms fluctuations of the drag and lift forces due to natural vortex shedding in a uniform flow with those in the presence of freestream turbulence. The values of C_x' and C_y' for the uniform and turbulent flow cases for the largest particle $d/\eta = 9.6$, $I = 0.1$, $\langle \mathrm{Re}_r \rangle = 609$ are 0.015 and 0.059, respectively. Consistent with previous observations, C_x' in the turbulent flow is nearly four times that in the uniform flow. In comparison, the values of C_y' for the two cases are 0.044 and 0.064, respectively, and therefore C_y' increases by only a factor of 1.5. Thus the fluctuations in the lift force are dominated by natural vortex shedding, while those in the drag force are substantially influenced by the freestream turbulence.

Cross-correlations between the DNS force and the ambient velocity are shown in Table V. They are computed as

$$\frac{\langle (C_x - \langle C_x \rangle)(U_x - \langle U_x \rangle) \rangle}{C_x' U_x'}, \quad \frac{\langle (C_y - \langle C_y \rangle)(U_y - \langle U_y \rangle) \rangle}{C_y' U_y'}, \tag{17}$$

for the x and y components, and similarly for the z component. For $d/\eta = 1.5$, the force response is strongly correlated to the freestream turbulence. The correlation decreases with increasing particle size and also with increasing turbulence intensity. Furthermore, in the case of larger particles, the cross-correlation is much less for the y and z components than for the x components. This is consistent with the previous observation that the lift force for the largest particle is generated due to the vortex shedding precess and not substantially influenced by the freestream turbulence, whereas the drag is strongly influenced by the freestream turbulence.

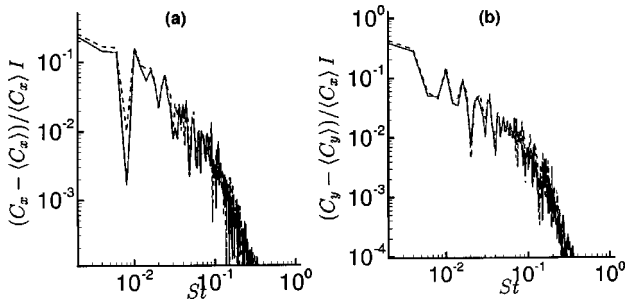

FIG. 13. Effect of increasing turbulence intensity at the same particle size. Spectra corresponding to Fig. 11 for $d/\eta = 1.5$. Symbols have the same meaning as in Fig. 11.

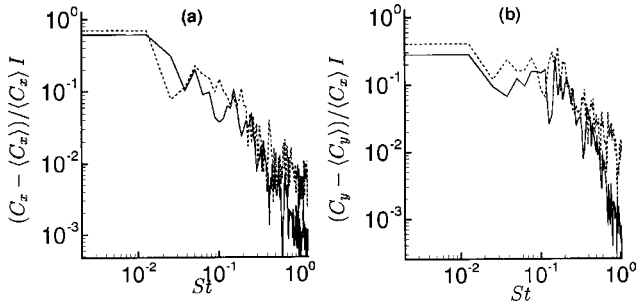

FIG. 14. Effect of increasing turbulence intensity at the same particle size. Spectra corresponding to Fig. 12 for $d/\eta = 9.6$. Symbols have the same meaning as in Fig. 12.

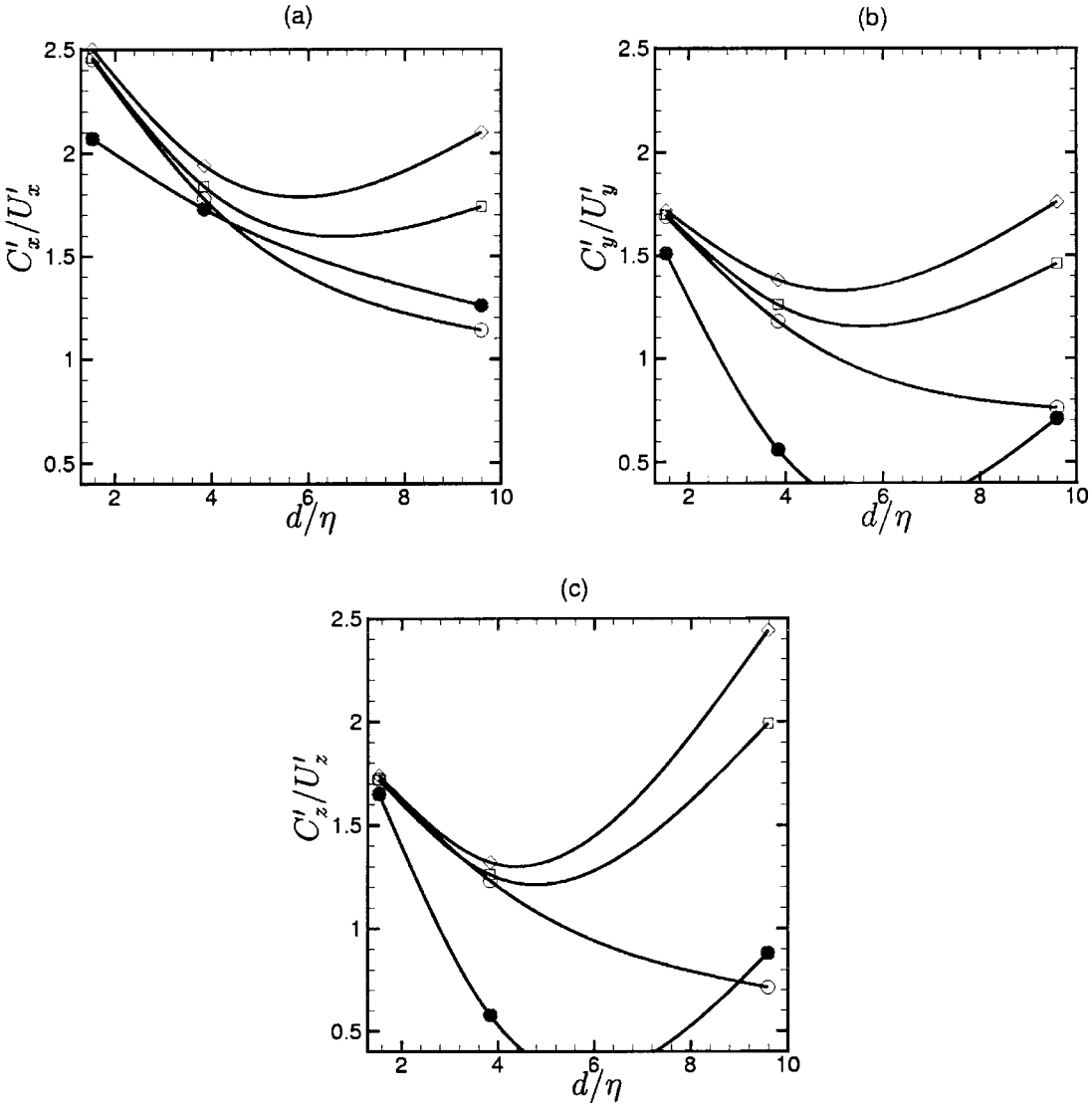

FIG. 15. rms of fluctuations in the force for $I=0.2$ or $I=0.25$. (●) DNS, (○) Schiller–Neumann law (2), (□) plus the inertial force, (◇) plus the history force.

E. Effect of intensity

The effect of increasing turbulence intensity while keeping the particle diameter fixed is shown in Fig. 11 for $d/\eta=1.5$ and in Fig. 12 for $d/\eta=9.6$. First of all, as the turbulence intensity (I) increases the mean drag increases, since the corresponding particle Reynolds number decreases as $1/I$. In the figures, the mean is subtracted from the time-dependent force and the fluctuations are presented after scaled by $\langle C_x\rangle I$. The plot for the $d/\eta=1.5$ case shows that the two cases of $I=0.1$ and 0.2 yield very similar fluctuations. The similarity of the two results should not be surprising since for the $I=0.1$ case the same box of isotropic turbulence is passed over at twice the speed as in the $I=0.2$ case. For the smallest particle ($d/\eta=1.5$), the low frequency responses collapse nearly perfectly, however some difference can be observed for the high frequency response. This result is consistent with the discussion given above that for the smallest particle, the drag and lift forces are well correlated with freestream turbulence. Thus the amplitude of fluctuation scales as $\langle C_x\rangle I$, and the scaling appears to be valid for all three components. For the largest particle at $d/\eta=9.6$, the fluctuations at $I=0.1$ and 0.25 are not similar. However, the overall intensity of fluctuations still appears to follow the above scaling.

The spectra of the time-dependent force corresponding to Figs. 11 and 12 are shown in Figs. 13 and 14, respectively. Similar observation as in the previous figures can be made. For the $d/\eta=1.5$ case, the frequency response is similar and the amplitude scales as $\langle C_x\rangle I$. For larger particles, however, the responses are dissimilar at different freestream intensities, however, the level of fluctuations follows the above scaling.

The rms of fluctuations in the drag and lift at the higher freestream intensity are shown in Fig. 15. Again, the rms of the force components are scaled by the corresponding rms of the freestream velocity as defined in (15) and (16). The DNS results show that the rms of C_x increases substantially for all particle sizes. The cross-stream force rms, however, does not

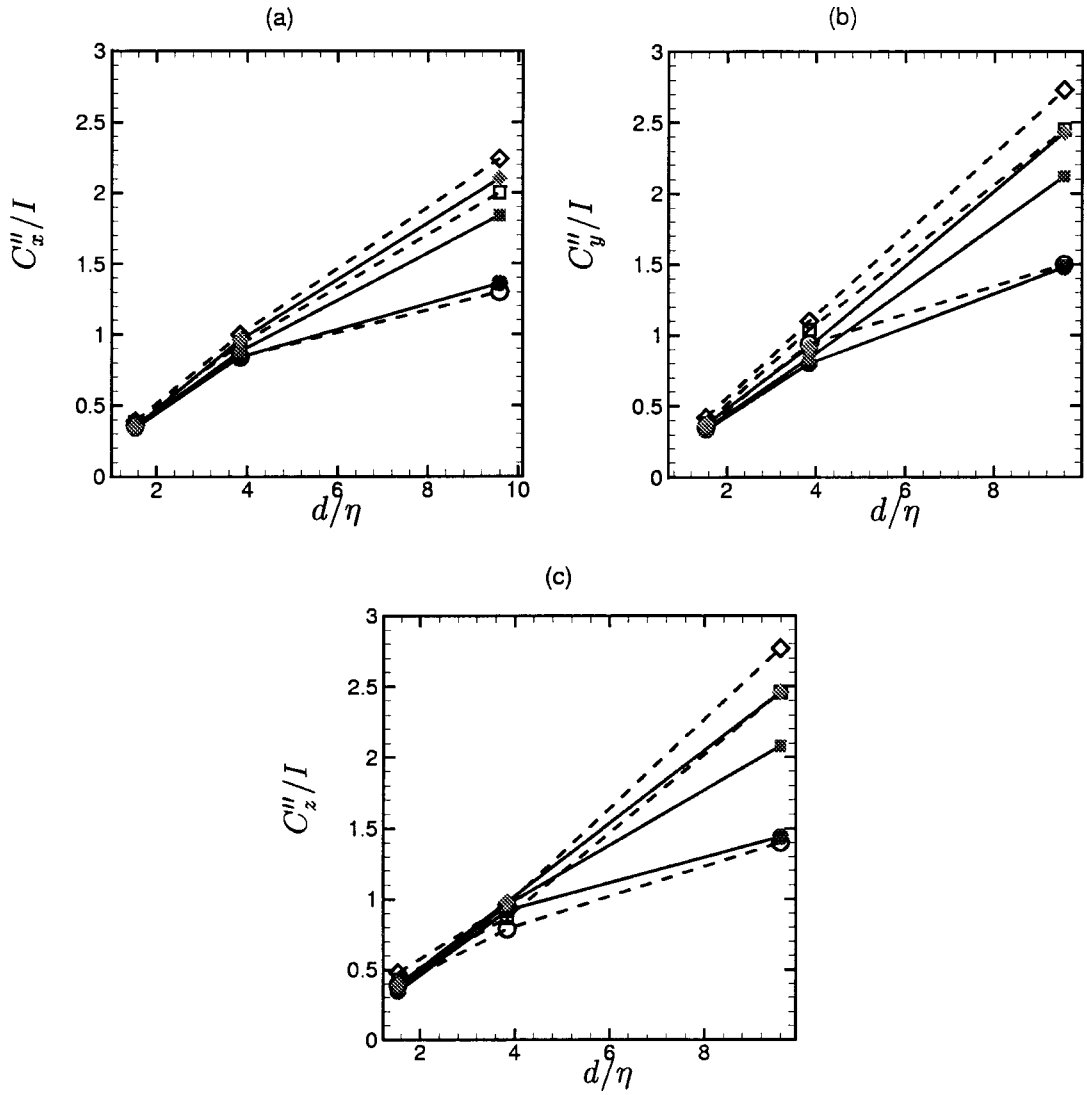

FIG. 16. Root-mean-square deviation of the DNS results from the predictions scaled by the freestream turbulence intensity. (○) Schiller–Neumann law, (□) plus the inertial force, (◇) plus the history force. The dashed lines and open symbols are for $I=0.1$, and the thick lines and solid symbols are for $I=0.2$ or $I=0.25$.

increase monotonically with d/η. For $d/\eta=1.5$, both C_y'/U_y' and C_z'/U_z' increase by nearly the same amount. Thus force fluctuations in the cross-stream directions are nearly axisymmetric about the wake centerline for the smallest particle at any freestream intensity. For the intermediate particle at $d/\eta=3.8$, the rms of the cross-stream fluctuations do not show any substantial change at $I=0.25$ compared to that at $I=0.1$. Thus for the intermediate particle, only the drag fluctuations increase. For the largest particle $d/\eta=9.6$, the rms of cross-stream fluctuations are actually reduced to about 75% of their values at $I=0.1$. Furthermore, unlike the lower intensity case ($I=0.1$), the case of higher intensity ($I=0.25$) shows that C_y'/U_y' and C_z'/U_z' are nearly the same. Thus with increasing freestream intensity the axisymmetric nature of the cross-stream fluctuations is recovered.

The rms fluctuations based on the different estimates are also shown in Fig. 15. The trend is similar to that observed earlier for the $I=0.1$ case. The Schiller–Neumann drag is the closest to the DNS results, except however, for the cross-stream fluctuations for the case of $d/\eta=3.8$ which are substantially reduced compared to the estimate. The inclusion of the added-mass and history forces does not have any substantial effect for $d/\eta=1.5$ and 3.8, but considerably increases the rms values at $d/\eta=9.6$ by introducing spurious oscillations.

The rms deviation of the different estimates from the corresponding DNS results is further illustrated by the normalized root-mean-square deviation defined as

$$C_x''=\frac{\langle (C_x-C_{x,\mathrm{DNS}})^2\rangle^{1/2}}{\langle C_{x,\mathrm{DNS}}\rangle},$$
$$C_y''=\frac{\langle (C_y-C_{y,\mathrm{DNS}})^2\rangle^{1/2}}{\langle C_{x,\mathrm{DNS}}\rangle}, \tag{18}$$
$$C_z''=\frac{\langle (C_z-C_{z,\mathrm{DNS}})^2\rangle^{1/2}}{\langle C_{x,\mathrm{DNS}}\rangle}.$$

These quantities are scaled by the freestream turbulence intensity I and shown in Fig. 16 as a function of the particle size. The figure shows that the rms deviation increases with

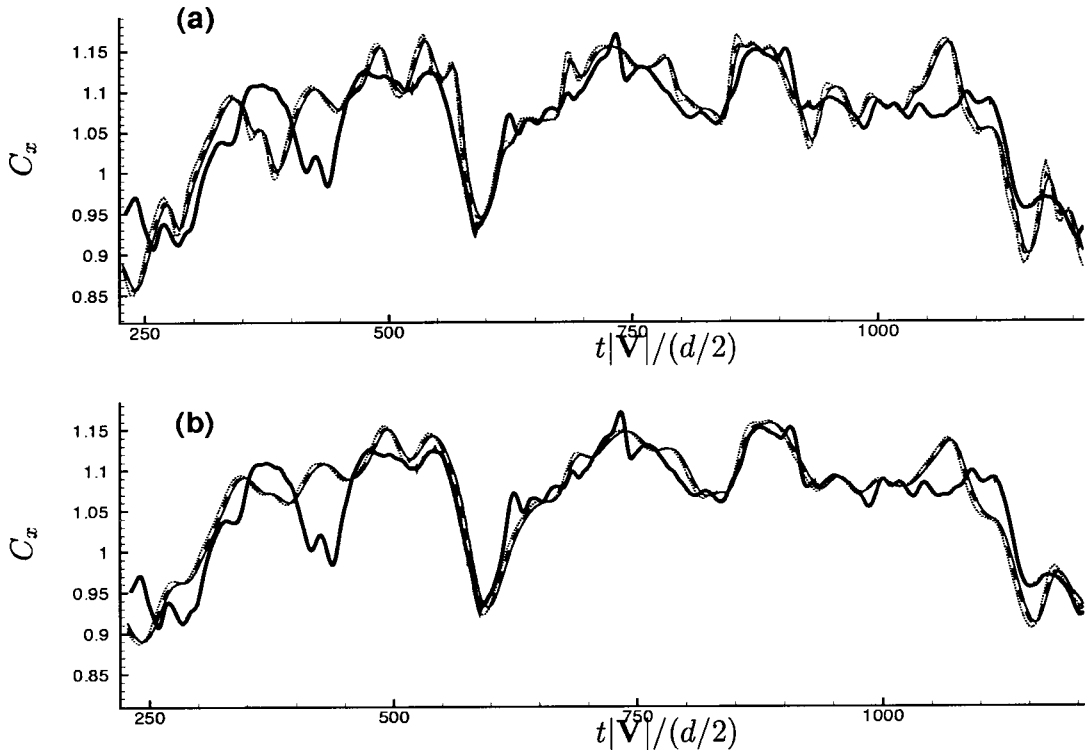

FIG. 17. C_x. $d/\eta=1.5$, $I=0.1$. Top: $2d$ average, bottom: $10d$ average. Thick line is the DNS result. (—) Schiller–Neumann drag, (---) with inertial force, $(\cdots)$ with history force.

the particle size and scales with I. It is also clear that the Schiller–Neumann drag law without the inertial and history contributions provides the closest approximation to the DNS results.

F. Estimates for fluid velocity

The use of the undisturbed fluid velocity at the center of the particle as the instantaneous fluid velocity seen by the

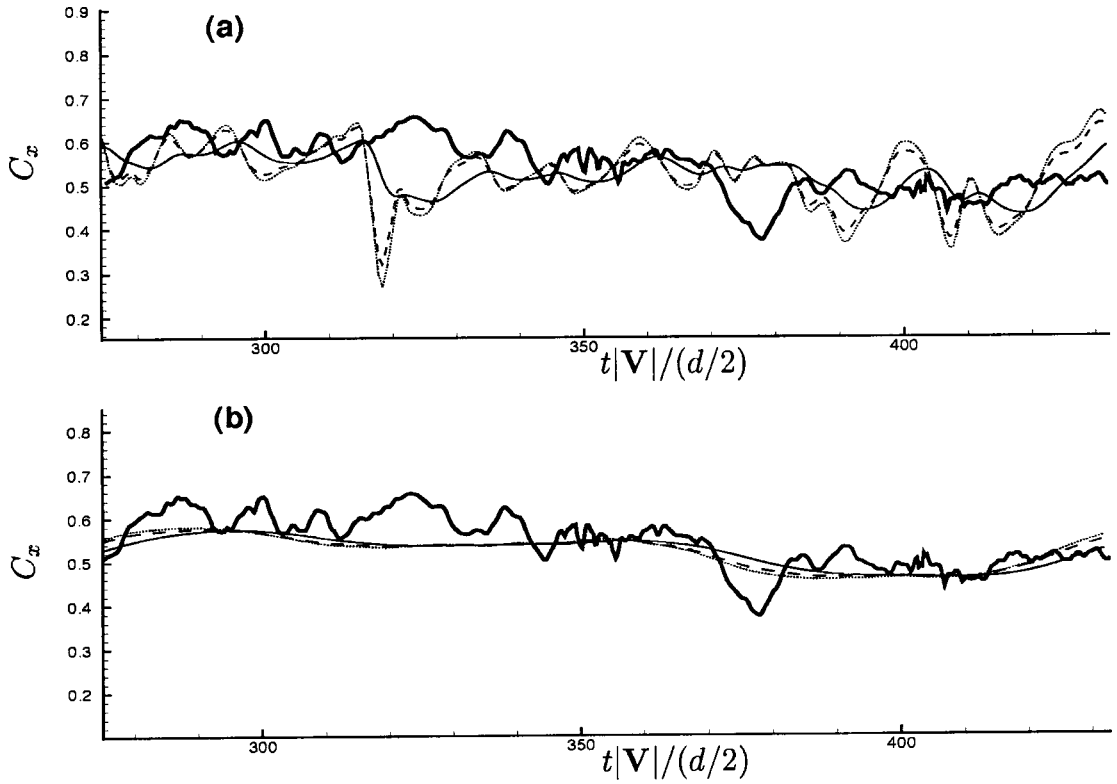

FIG. 18. C_x. $d/\eta=9.6$. Top: $1.2d$ average, bottom: $10d$ average. Symbols have same meaning as in Fig. 17.

TABLE VI. Mean drag by using different volume-averaged estimates for the fluid velocity. $d/\eta=9.6$, $I=0.1$, $\langle \mathrm{Re}_r\rangle=609$ (case 5). Mean drag is unaffected by the estimates and by addition of the added-mass and history forces based on those estimates.

	$1.2d$	$10d$
Schiller–Neumann	0.532	0.529
Schiller–Neumann + inertial force	0.532	0.529
Schiller–Neumann + inertial force + history force	0.529	0.529

particle can be questioned. This definition is appropriate for a particle much smaller than the Kolmogorov scale, but for particles of larger size, the definition of the fluid velocity in the various estimates must be reconsidered. A simple approach is to define the instantaneous fluid velocity based on a volume average of the undisturbed ambient flow around the particle. The added-mass and history forces as given in (14) can then be computed using this volume-averaged fluid velocity. The estimates of Schiller–Neumann drag thus computed are plotted in Fig. 17 for $d/\eta=1.5$, $I=0.1$, $\langle \mathrm{Re}_r\rangle=107$ (case 1) for two different approximations of the fluid velocity seen by the particle: one obtained by averaging the undisturbed fluid over a volume of 2 times the particle diameter and the other obtained by averaging over 10 times the particle diameter. Also plotted for comparison are the DNS data and estimates that include the inertial and history contributions based on the volume-averaged fluid velocity. The results for case 5 ($d/\eta=9.6, I=0.1, \langle \mathrm{Re}_r\rangle=609$) using averaging volumes of size 1.2 and 10 times the particle diameter are shown in Fig. 18.

Expectedly, with increasing size of the volume of averaging, the time variation in the estimated force decreases. In particular, the high frequency components are significantly diminished. As a result the inertial and history contributions are also suppressed. For the different cases shown the mean drag remains virtually unaffected by the size of the averaging volume (Table VI). Of course, in the limit when the volume of averaging becomes as large as the box of turbulence the fluid velocity seen by the particle becomes a constant equal to $\mathbf{V}$ and the corresponding drag estimate reduces to (12), resulting in a substantially different estimation of the mean drag (see estimate 3 in Table III).

The rms fluctuation of C_x and C_y obtained by using the above volume-averaged estimates are shown in Fig. 19 as a function of the size of the averaging volume. The rms fluctuations are computed using (15). The rms of the DNS result is also shown. For the smallest particle the comparison of the rms fluctuation with the DNS data improves as the size of the averaging volume increases. However, for the larger particles, the rms fluctuation in the Schiller–Neumann estimation is lower than the DNS result even when the fluid velocity is taken to be at the center of the particle. With increasing size of the averaging volume the rms fluctuation in the

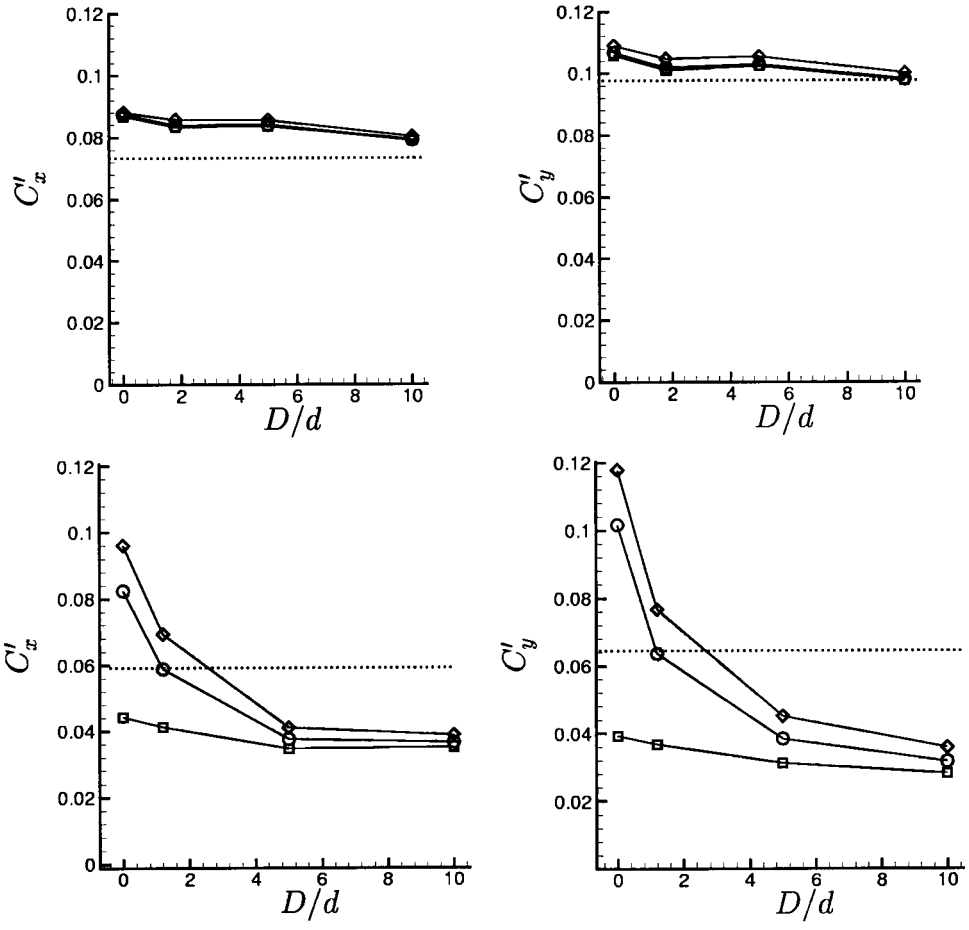

FIG. 19. rms of C_x (left panel) and C_y (right panel) based on different volume-averaged estimates for the fluid velocity. D is the diameter of the volume of averaging. Top: $d/\eta=1.5$, $I=0.1$, $\langle \mathrm{Re}_r\rangle=107$; bottom: $d/\eta=9.6$, $I=0.1$, $\langle \mathrm{Re}_r\rangle=609$. The dotted line indicates the DNS result. (□) Schiller–Neumann; (○) with inertial force; (◇) with inertial and history force. $D/d=0$ indicates the undisturbed fluid velocity measured at the center of the particle.

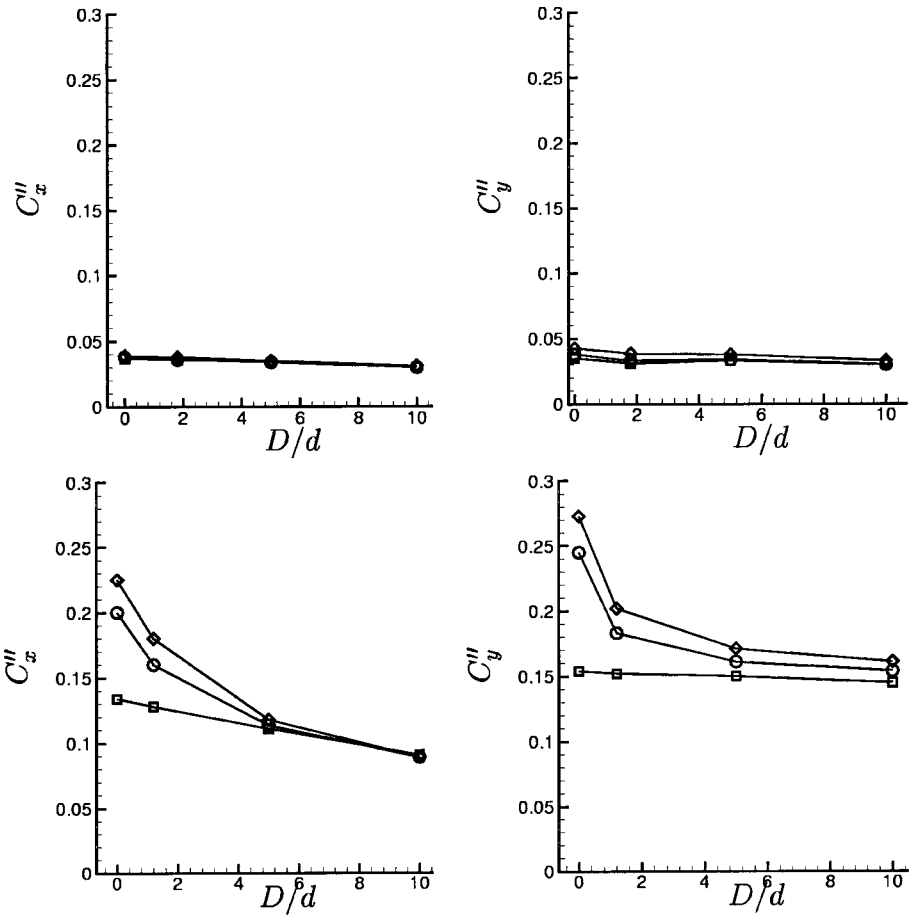

FIG. 20. Root-mean-square deviation from the DNS results of predictions using different volume-averaged estimates for fluid velocity. Top: $d/\eta = 1.5$, $I = 0.1$, $\langle \mathrm{Re}_r \rangle = 107$; bottom: $d/\eta = 9.6$, $I = 0.1$, $\langle \mathrm{Re}_r \rangle = 609$. Symbols: (□) Schiller–Neumann; (○) with inertial force; (◇) with the inertial and history forces.

Schiller–Neumann estimation further decreases. Note that the larger particle is about 6.5 times bigger than the smaller particle. The inclusion of the inertial and history forces increases the level of fluctuation, however, these fluctuations do not necessarily reflect the actual behavior. With increasing size of the averaging volume these fluctuations diminish, and the difference from the Schiller–Neumann estimation decreases. This fact is illustrated by computing the rms deviation in the different estimates from the corresponding true DNS results as given in (18). These results as a function of the size of the averaging volume for two different cases are shown in Fig. 20. It is clear that the Schiller–Neumann drag law without the inertial and history contributions provides the closest approximation to the DNS results.

IV. SUMMARY AND CONCLUSIONS

The purpose of this paper is to address the effect of freestream turbulence on the drag force on a particle. We consider direct numerical simulation of a particle subjected to a frozen isotropic turbulent flow. The particle Reynolds number is about 50–600, the diameter is about 1.5–10 times the Kolmogorov scale, and the freestream turbulence intensity is about 10%–25%. We compare the DNS results on the mean and time-dependent drag with the predictions based on the standard drag correlation, and those including the added-mass and history forces.

We observe that the freestream turbulence does not have a systematic and substantial effect on the mean drag. The standard drag correlation based on the instantaneous or mean relative velocity yields a reasonably accurate prediction of the mean drag obtained from the DNS. The mean drag however depends on the definition of the mean fluid velocity. The mean fluid velocity obtained by averaging over the entire volume of fluid can result in a significantly different value of the mean drag if the particle does not sample the entire volume.

The accuracy of prediction of the instantaneous drag force decreases with increasing particle size. For the smallest particle, the low frequency oscillations in the DNS drag are well captured by the standard drag, but for the larger particles significant differences exist even for the low frequency components. For the smallest particle, the cross-correlation between the DNS drag and the freestream velocity is the highest, and it decreases with increasing particle size.

Inclusion of the added-mass and history forces does not improve the prediction, and for the larger particles these forces introduce spurious oscillations not observed in the DNS. Analysis of the rms fluctuations suggests that the standard drag correlation provides the closest approximation for the DNS results.

The fluctuations in the cross-stream forces are statistically axisymmetric about the wake centerline for the smallest particle but not for the larger particles, where vortex shedding begins to play a role. For the largest particle, the effect of freestream turbulence is stronger on the streamwise force than on the cross-stream forces, which are dominated by

natural vortex shedding. The cross-stream forces become axisymmetric as the freestream intensity increases, which begins to suppress natural vortex shedding.

We observe the magnitude of fluctuations in the drag and lift forces to scale linearly with both the mean drag and freestream turbulence intensity, i.e., $C_x', C_y', C_z' \propto I(1 + 0.15\,\mathrm{Re}^{0.687})\mathrm{Re}^{-1}$.

Since the use of the undisturbed fluid velocity measured at the center of the particle as the fluid velocity seen by the particle is *ad hoc*, we examine various approximations to the fluid velocity obtained by averaging over a volume of fluid around the particle. It is shown that the mean drag is insensitive to the definition of the mean fluid velocity, as far as the latter is defined either based on the undisturbed fluid velocity at the center of the particle, or based on an estimate obtained by averaging over a fluid volume of the order of the particle size. The fluctuations diminish as the volume of averaging increases. The overall conclusion is that the standard drag correlation without the added-mass and history forces provides the closest approximation to the DNS result.

ACKNOWLEDGMENTS

The research is supported by the ASCI Center for Simulation of Advanced Rockets at the University of Illinois at Urbana–Champaign through the U.S. Department of Energy (B341494). Computational facilities from the National Center for Supercomputing Applications, UIUC are greatly acknowledged. Thanks are also due to Dr. J. P. Ferry and Dr. F. M. Najjar.

[1] R. Mei, R. J. Adrian, and T. J. Hanratty, "Particle dispersion in isotropic turbulence under Stokes drag and Basset force with gravitational settling," J. Fluid Mech. **225**, 481 (1991).
[2] L.-P. Wang and M. R. Maxey, "Settling velocity and concentration distribution of heavy particles in homogeneous isotropic turbulence," J. Fluid Mech. **256**, 27 (1993).
[3] P. H. T. Uhlherr and C. G. Sinclair, "The effect of freestream turbulence on the drag coefficients of spheres," Proc. CHEMECA **1**, 1 (1970).
[4] N. A. Zarin and J. A. Nicholls, "Sphere drag in solid rockets—noncontinuum and turbulence effects," Combust. Sci. Technol. **3**, 273 (1971).
[5] A. Brucato, F. Grisafi, and G. Montante, "Particle drag coefficients in turbulent fluids," Chem. Eng. Sci. **53**, 3295 (1998).
[6] J. Yusof, "Interaction of massive particles with turbulence," Ph.D. thesis, Department of Mechanical Engineering, Cornell University, 1996.
[7] R. R. Rudolff and W. D. Bachalo, "Measurement of droplet drag coefficients in polydispersed turbulent flow field," AIAA Pap. 88-0235 (1988).
[8] W. D. Warnica, M. Renksizbulut, and A. B. Strong, "Drag coefficient of spherical liquid droplets," Exp. Fluids **18**, 265 (1994).
[9] J.-S. Wu and G. M. Faeth, "Sphere wakes at moderate Reynolds numbers in a turbulent environment," AIAA J. **32**, 535 (1994).
[10] J.-S. Wu and G. M. Faeth, "Effect of ambient turbulence intensity on sphere wakes at intermediate Reynolds numbers," AIAA J. **33**, 171 (1994).
[11] L. B. Torobin and W. H. Gauvin, "Fundamental aspects of solid-gas flow. 1," Can. J. Chem. Eng. **38**, 129 (1959).
[12] L. B. Torobin and W. H. Gauvin, "Drag coefficients of single spheres moving in steady and accelerated motion in a turbulent fluid," AIChE J. **7**, 615 (1961).
[13] A. Clamen and W. H. Gauvin, "Effect of turbulence on the drag coefficients of spheres in a supercritical flow regime," AIChE J. **15**, 184 (1969).
[14] R. Clift and W. H. Gauvin, "The motion of particles in turbulent gas streams," Proc. CHEMECA **1**, 14 (1970).
[15] R. A. Gore and C. T. Crowe, "Discussion of 'Particle drag in a dilute turbulent two-phase suspension flow,' " Int. J. Multiphase Flow **16**, 359 (1990).
[16] S. Sankagiri and G. A. Ruff, "Measurement of sphere drag in high turbulence intensity flows," Proc. ASME Fluids Eng. Div. **244**, 277 (1997).
[17] R. Mittal, "Response of the sphere wake to freestream fluctuations," Theor. Comput. Fluid Dyn. **13**, 397 (2000).
[18] R. Clift, J. R. Grace, and M. E. Weber, *Bubbles, Drops and Particles* (Academic, New York, 1978).
[19] J. A. Langford, "Toward ideal larger-eddy simulation," Ph.D. thesis, Department of Theoretical and Applied Mechanics, University of Illinois at Urbana–Champaign, Urbana, IL (2000).
[20] P. Bagchi and S. Balachandar, "Steady planar straining flow past a rigid sphere at moderate Reynolds number," J. Fluid Mech. **466**, 365 (2002).
[21] R. Mittal and S. Balachandar, "Direct numerical simulation of flow past elliptic cylinders," J. Comput. Phys. **124**, 351 (1996).
[22] Y. Tsuji, Y. Morikawa, and H. Shiomi, "LDV measurement of an air-solid two-phase flow in a vertical pipe," J. Fluid Mech. **139**, 417 (1984).
[23] M. Mizukami, R. N. Parthasarathy, and G. M. Faeth, "Particle generated turbulence in homogeneous dilute dispersed flow," Int. J. Multiphase Flow **18**, 397 (1992).
[24] R. N. Parthasarathy and G. M. Faeth, "Turbulence modulation in homogeneous dilute particle-laden flows," J. Fluid Mech. **220**, 485 (1990).
[25] Y. Tsuji, Y. Morikawa, T. Tanaka, K. Karimine, and S. Nishida, "Measurement of an axisymmetric jet laden with coarse particles," Int. J. Multiphase Flow **14**, 565 (1988).
[26] E. K. Longmire and J. K. Eaton, "Structure of a particle-laden round jet," J. Fluid Mech. **236**, 217 (1992).
[27] J. D. Kulick, J. R. Fessler, and J. K. Eaton, "Particle response and turbulence modification in fully developed channel flow," J. Fluid Mech. **277**, 109 (1994).
[28] P. Bagchi and S. Balachandar, "Effect of free rotation on the motion of a solid sphere in linear shear flow at moderate Re," Phys. Fluids **14**, 2719 (2002).
[29] P. Bagchi and S. Balachandar, "Shear versus vortex-induced lift force on a rigid sphere at moderate Re," J. Fluid Mech. **473**, 379 (2002).
[30] P. Bagchi and S. Balachandar, "Inertial and viscous forces on a rigid sphere in straining flows at moderate Reynolds numbers," J. Fluid Mech. **481**, 105 (2003).
[31] P. Bagchi, "Particle dynamics in inhomogeneous flows at moderate to high Reynolds numbers," Ph.D. thesis, Department of Theoretical and Applied Mechanics, University of Illinois at Urbana–Champaign (2002).
[32] R. Mittal, "A Fourier Chebyshev spectral collocation method for simulation flow past spheres and spheroids," Int. J. Numer. Methods Fluids **30**, 921 (1999).
[33] J. Magnaudet, M. Rivero, and J. Fabre, "Accelerated flows past a rigid sphere or a spherical bubble. Part 1. Steady straining flow," J. Fluid Mech. **284**, 97 (1995).
[34] L. Schiller and A. Neumann, "Uber die grundlegenden Berechungen bei der Schwer kraftaufbereitung," Verein Deutscher Ingenieure **77**, 318 (1933).
[35] R. Mei and R. J. Adrian, "Flow past a sphere with an oscillation in the free-stream and unsteady drag at finite Reynolds number," J. Fluid Mech. **237**, 133 (1992).